AGU PUBLICATIONS

JGR

Journal of Geophysical Research: Oceans

RESEARCH ARTICLE

10.1002/2015JC011413

Causes for intraseasonal sea surface salinity variability in the western tropical Pacific Ocean and its seasonality

Yuanlong Li[1] and Weiqing Han[1]

[1]Department of Atmospheric and Oceanic Sciences, University of Colorado, Boulder, Colorado, USA

Key Points:
- Intraseasonal SSS variability is pronounced in the western tropical Pacific
- Wind stress-driven ocean dynamics and precipitation are major causes
- Mixed-layer thickness is crucial in determining the amplitude of SSS variability

Correspondence to:
Y. Li,
yuanlong.li@colorado.edu

Citation:
Li, Y., and W. Han (2016), Causes for intraseasonal sea surface salinity variability in the western tropical Pacific Ocean and its seasonality, *J. Geophys. Res. Oceans*, *121*, 85–103, doi:10.1002/2015JC011413.

Received 23 OCT 2015
Accepted 7 DEC 2015
Accepted article online14 DEC 2015
Published online 8 JAN 2016

Abstract Pronounced intraseasonal variability (ISV; 20–90 day) of sea surface salinity (SSS) with a standard deviation of 0.12–0.20 psu is detected in the western tropical Pacific Ocean (PO) from measurements of Aquarius/SAC-D satellite. These variations are not spatially uniform but show distinct regional features. The Hybrid Coordinate Ocean Model (HYCOM) well simulated the observed SSS variations, and a suite of parallel experiments were performed to understand the underlying physical processes. Surface forcing by atmospheric intraseasonal oscillations which are dominated by the Madden-Julian oscillation (MJO) is largely responsible for producing the SSS ISV, while ocean internal variability plays a secondary role. Impact of atmospheric forcing is primarily through precipitation and wind stress-driven oceanic processes. Their relative importance shows spatial variations. They have approximately equal importance in the western equatorial PO west of 155°E and the southwestern tropical PO. Wind stress effect dominates SSS ISV in the equatorial PO east of 155°E, while precipitation effect is larger in the northwestern tropical PO. In comparison, the effect of evaporation induced by wind speed change is smaller. The SSS ISV also shows evident seasonality in some areas, particularly in the far western equatorial basin and southwestern tropical PO. During boreal summer (winter), SSS ISV is enhanced (weakened) in the northwestern PO and weakened (enhanced) in the southwestern PO. Comparing with the strength of atmospheric forcing, seasonal variation of the ocean state, especially the mixed layer depth, is generally more important in causing such seasonality.

1. Introduction

Ocean salinity is a fundamental physical property of sea water, which influences the stratification and circulation of the world ocean. It also serves as a potential indicator of the global water cycle [e.g., *Lagerloef et al.*, 1995; *Yu*, 2011]. Ocean salinity plays a vital role in the tropical ocean dynamics and air-sea interaction. Particularly, the large vertical salinity gradient in the western tropical Pacific Ocean (PO) gives rise to a barrier layer which inhibits vertical entrainment cooling and helps to maintain the high heat content of the western Pacific warm pool [*Lukas and Lindstrom*, 1991; *Sprintall and Tomczak*, 1992]. Variability of the upper-ocean salinity and barrier layer can significantly affect the local mixed layer heat budget and thereby influence the evolution of El Niño–Southern Oscillation (ENSO) [e.g., *Picaut et al.*, 1996; *Maes et al.*, 2005; *Zhu et al.*, 2014]. Consequently, investigating ocean salinity variability in the western tropical PO will contribute to our understanding of tropical climate variability.

Previous studies on sea surface salinity (SSS) variations in the western tropical PO were primarily based on in-situ observations. On seasonal timescale, large SSS variations were seen in the inter-tropical convergence zone (ITCZ) and South Pacific convergence zone (SPCZ) regions, which are mainly controlled by rainfall changes [e.g., *Delcroix and Henin*,1991; *Delcroix et al.*, 1996, 2014; *Hénin et al.*, 1998]. On interannual timescale, SSS variations have larger amplitudes with more complicated spatial patterns than seasonal variability, and they are closely related to ENSO variability through changes in freshwater flux and wind-driven ocean current advection [e.g., *Delcroix and Picaut*, 1998; *Maes*, 2000; *Delcroix and McPhaden*, 2002; *Singh et al.*, 2011; *Hasson et al.*, 2013]. Recent studies also reveal decadal and multidecadal SSS fluctuations with a freshening trend in the western tropical PO, which are likely caused by freshwater flux that is linked to the slow change of the global water cycle [*Delcroix et al.*, 2007; *Cravatte et al.*, 2009; *Skliris et al.*, 2014]. In comparison, intraseasonal variability (ISV) of SSS in this region is rarely investigated due to the lack of observational data and difficulties in model simulation. Particularly, the lack of high-quality precipitation and surface wind data makes the simulation of SSS challenging for existing ocean general circulation models

(OGCMs) [*Joualalen et al*., 2003; *Wang and Chao*, 2004; *Felton et al*., 2014]. The western tropical PO is however subjected to strong impact of atmospheric intraseasonal oscillations, such as the Madden-Julian oscillations (MJOs) [*Madden and Julian*, 1971], which can induce large ISV in upper-ocean salinity. For example, pronounced salinity ISV was detected in the moored buoy records [*Ueki et al*., 2002; *Kashino et al*., 2011] and Argo float data [*Matthews et al*., 2010].

The space-borne SSS measurements of the Soil Moisture Ocean Salinity (SMOS) [*Font et al*., 2010] and Aquarius/SAC-D (Satellite de Application Cientificas-D) [*Lagerloef et al*., 1995, 2008] satellites in the past several years have provided a revolutionary ability for monitoring and understanding basin-wide SSS variability. These satellite SSS data have been successfully utilized in investigating surface water masses [e.g., *Bingham et al*., 2014; *Dohan et al*., 2015; *Sabia et al*., 2014; *Yu*, 2014], salinity structures in marginal seas [*Grodsky et al*., 2014; *Gierach et al*., 2013; *Kim et al*., 2014; *Zeng et al*., 2014], salt stratification near the sea surface [*Felton et al*., 2014; *Moon and Song*, 2014; *Song et al*., 2015], evolution of ENSO events [*Hasson et al*., 2014; *Qu and Yu*, 2014; *Qu et al*., 2014], salinity signatures of the tropical instability waves [*Lee et al*., 2012, 2014], ocean salinity fronts [*Kao and Lagerloef*, 2015; *Yu*, 2015], and western boundary currents [*Reul et al*., 2014]. These researches have effectively integrated our knowledge of salinity-related ocean phenomena. More importantly, Aquarius SSS data are capable of capturing intraseasonal anomalies of SSS in the tropical Oceans. *Shinoda et al*. [2013] found that Aquarius data can well represent the SSS variations during three MJO events occurred in the 2011–2012 winter. *Grunseich et al*. [2013] identified well-organized MJO signals in Aquarius SSS data across the equatorial Indo-Pacific Ocean following the MJO precipitation fluctuations. *Guan et al*. [2014] showed that Aquarius-measured SSS is out of phase with freshwater flux in the western equatorial PO between 155°E and 165°E during MJO events. They argued that ocean dynamics might be important in causing the observed SSS variations. *Li et al*. [2015] investigated SSS ISV in the equatorial (5°S–5°N) Indo-Pacific Ocean through OGCM experiments and found that external forcing by atmospheric intraseasonal oscillations, which are dominated by the MJO, is the primary cause for SSS ISV. They also demonstrated that in most of the equatorial Indo-Pacific basin wind stress-driven ocean processes play a more important role than precipitation.

The standard deviation (STD) of the 20–90 day band-pass filtered SSS in Figure 1a is based on Aquarius Combined Active-Passive (CAP) data from October 2011 through October 2014, as a measure of the overall intensity of SSS ISV. Large STD values of $\sim$0.20 psu occur in the western equatorial PO and extend in three directions, northwestward to the Philippine Sea, eastward to a slanted zonal band across Pacific basin between 2°N and 10°N which is roughly along the ITCZ, and southeastward to the SPCZ region. As a result, the entire 10°S–10°N region of the western tropical PO is characterized by pronounced SSS ISV with STDs $>$ 0.12 psu. These variations are however not spatially uniform, as indicated by the leading two empirical orthogonal function (EOF) modes of 20–90 day SSS in the high-STD region (Figures 2a and 2b). The first mode displays a zonal dipole pattern along the equator, with out-of-phase anomalies between the far western equatorial PO (west of 150°E) and the area east of 160°E (Figure 2a). The second mode has positive anomalies along the equator and negative ones in the northwestern tropical PO (Figure 2b). Although these two modes, which explain 10.9% and 8.9% of the total variance, are not significantly separated from each other and from the remaining variance (the third mode explains 7.4%) according to the North's significant test [*North et al*., 1982], they do imply a complicated spatial structure of intraseasonal SSS variability in the western tropical PO. Variations in different areas could be generated by different mechanisms. Note that *Guan et al*. [2014] and *Li et al*. [2015] mainly studied the box area of 155°E–165°E, 5°S–5°N. A comprehensive investigation of SSS ISV for the entire western tropical PO has not yet been done.

In this study, we expand the work of *Li et al*. [2015] to the entire western tropical PO and focus on two issues. First, we study the spatial variation of SSS ISV. We will describe and compare the characteristics and mechanisms of ISV in different areas. Second, we investigate the seasonality of SSS ISV. We will quantify the seasonal variation of ISV amplitude and explore its causes. To achieve these objectives, we analyze Aquarius SSS data and perform OGCM experiments. The rest of the paper is organized as follows. Section 2 describes the data and model. Section 3 presents the results of our analyses. Specifically, section 3.1 evaluates HYCOM performance in the western tropical PO, section 3.2 explores the mechanisms of SSS ISV by assessing effects of different processes, and section 3.3 examines the seasonality of SSS ISV. Finally, section 4 provides a summary and discussion.

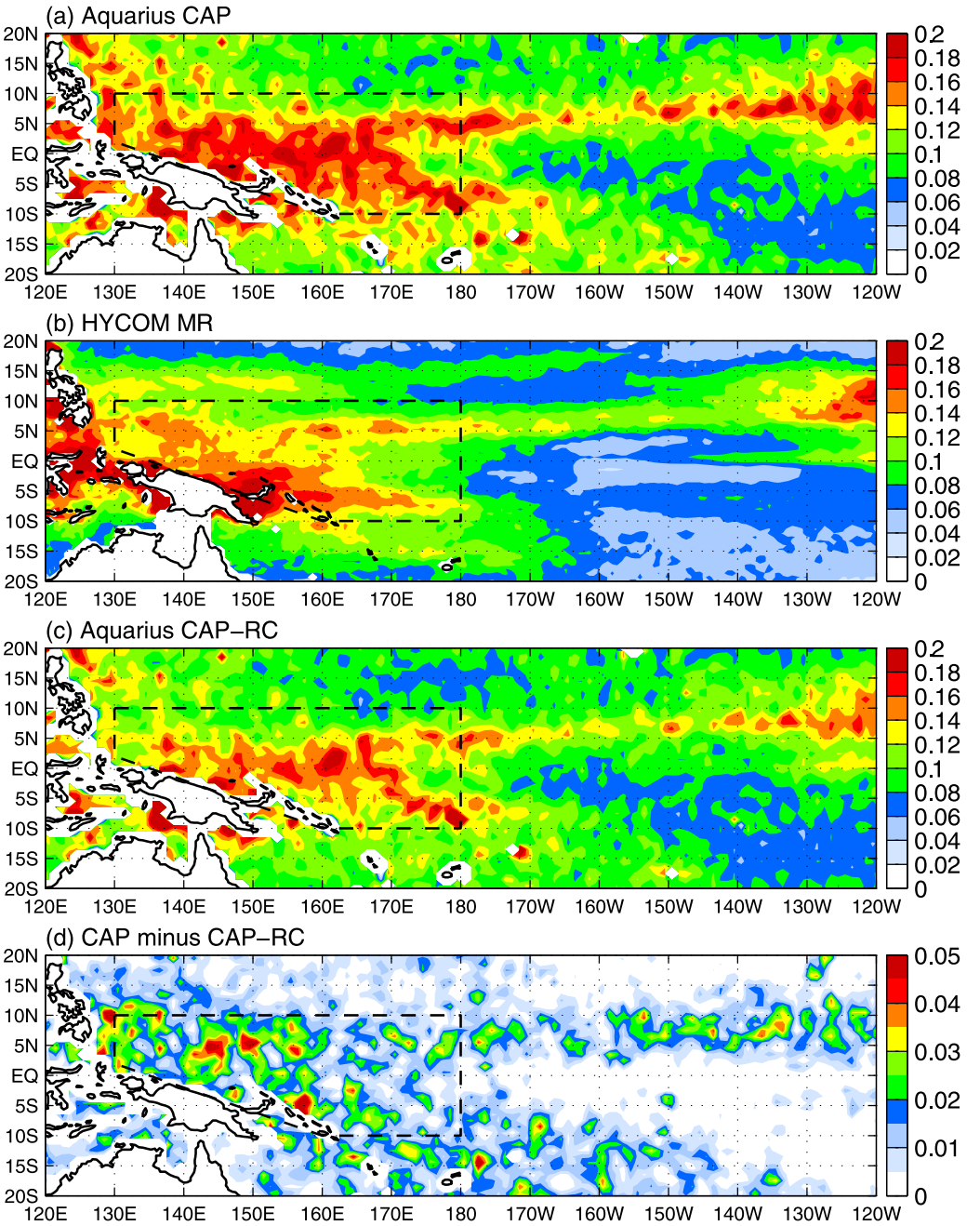

Figure 1. Standard deviation (STD) maps of the 20–90 day band-pass filtered SSS (psu) based on (a) Aquarius CAP data during October 2011 to October 2014, (b) HYCOM MR output during February 2002 to October 2011, and (c) Aquarius CAP-RC data during October 2011 to October 2014. (d) The difference in 20–90 day SSS STD (psu) between Aquarius CAP and CAP-RC data. The dashed lines mark the high-STD area (130°E–180°E, 10°S–10°N).

2. Data and Model

2.1. Observational Data

The Aquarius satellite was launched on the SAC-D spacecraft in June 2011 [*Lagerloef et al.*, 1995, 2008]. It provides SSS estimates with a spatial resolution of 150 km and a target retrieval accuracy of 0.2 psu on monthly timescale. In this study we mainly analyze the Version-3.0 Aquarius Combined Active-Passive retrieval (CAP) Level 3 product [*Yueh et al.*, 2013, 2014] from August 2011 through November 2014. The CAP

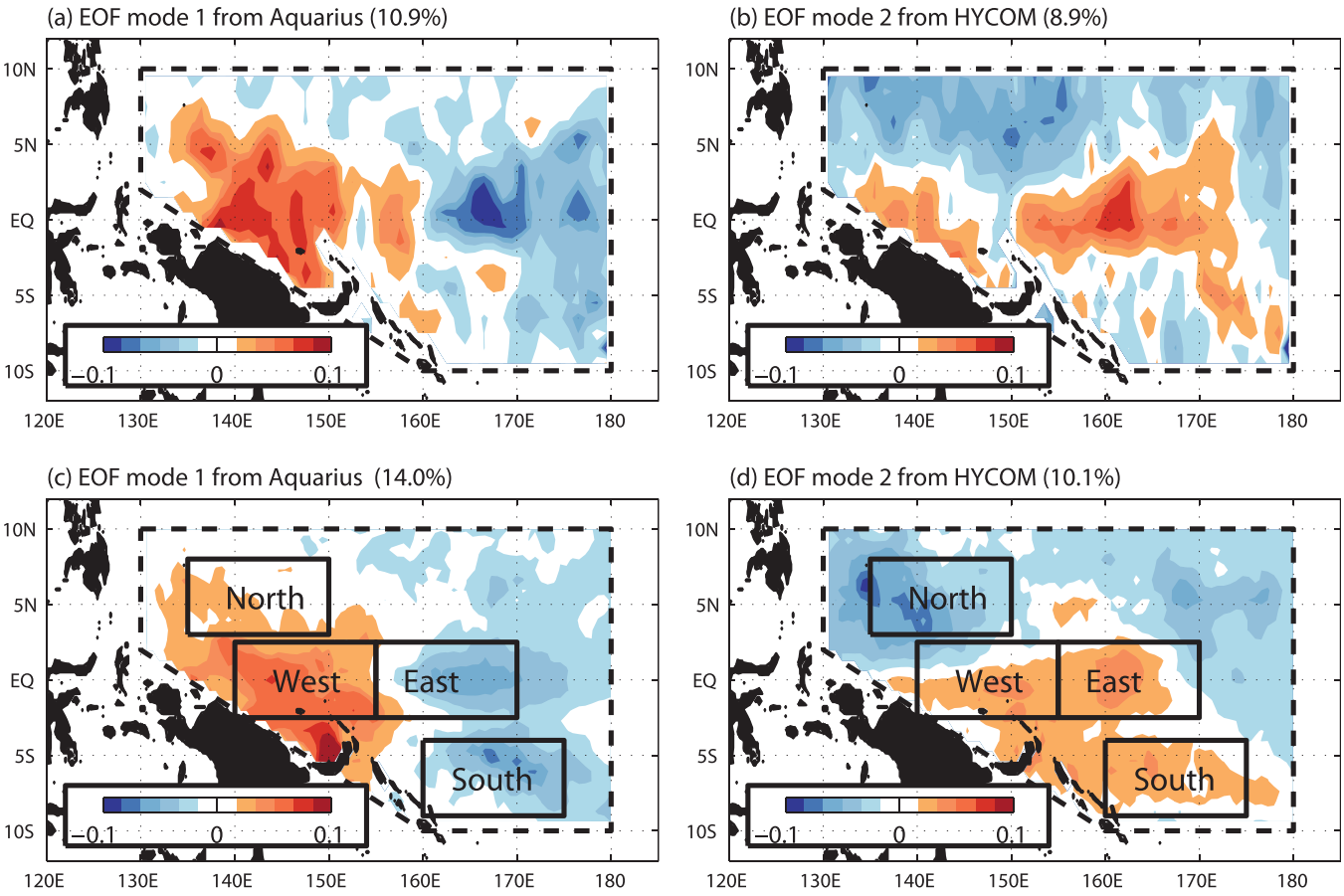

Figure 2. (a) The first and (b) the second EOF modes for the 20–90 day SSS from Aquarius CAP data for the October 2011 to October 2014 period, which explain 10.9% and 8.9% of the total variance. The EOF analysis is performed for the high-STD region identified in Figure 1. (c and d) similar to Figures 2a and 2b but based on HYCOM MR output for the February 2002 to October 2011 period. The black rectangles in Figures 2c and 2d denote the western, the eastern, the northern, and the southern boxes.

algorithm simultaneously retrieves salinity, wind speed, and wind direction by minimizing the sum of squared differences between the retrieval model and observations [*Yueh et al.*, 2014]. This product provides 1° × 1° gridded, 7 day running-mean SSS data at daily intervals. Another version of Aquarius product, the Version-3.0 CAP Level 3 SSS with rain correction (CAP-RC) [*Yueh et al.*, 2013; *Tang et al.*, 2014], is recently released. Comparing with CAP SSS, CAP-RC SSS tends to be closer to the surface salinity from in-situ observations and model results. However, as the rain correction issue is still an area of continuing research, the difference between CAP-RC and CAP is considered as "uncertainty" rather than an improvement in the retrieved SSS value [*Tang et al.*, 2014]. Here we use CAP-RC data to evaluate the rain-induced uncertainty in SSS ISV in the heavy-rainfall western tropical PO.

Other observational data sets used in our analyses are the 1°×1° Grid Point Value of the Monthly Objective Analysis (MOAA GPV) [*Hosoda et al.*, 2008] of temperature and salinity based on Argo data and other in-situ observations, the 0.25°×0.25° daily Cross-Calibrated Multi-Platform (CCMP) 10 m wind vector data [*Atlas et al.*, 2008], the 0.25°×0.25° daily Tropical Rainfall Measuring Mission (TRMM) Multi-Satellite Precipitation Analysis (TMPA) level 3B42 precipitation product [*Huffman et al.*, 2007], and the 1/3° × 1/3°, 5 day satellite-based ocean surface current estimate from Ocean Surface Current Analysis-Real time (OSCAR) product [*Bonjean and Lagerloef*, 2002] during 2002–2011.

2.2. Ocean Model and Experiments

The Hybrid Coordinate Ocean Model (HYCOM) combines isopycnal, sigma (terrain-following), and *z*-level coordinates to optimize the representation of oceanic processes [*Bleck*, 2002]. The version-2.2.18 HYCOM has been successfully utilized to investigate intraseasonal oceanic variations in the tropical Indian and

Table 1. A Summary of HYCOM Model Experiments[a]

Solution	Forcing	Description
MR	daily forcing	complete solution
NoMJO	(105 day) low-passed forcing	remove all MJO effects
NoP	low-passed precipitation	remove MJO precipitation effect
NoWND	low-passed wind speed/stress	remove MJO total wind effect
NoTAU	low-passed wind stress	remove MJO wind stress effect
NoSeason	(120 day) high-passed forcing	remove seasonal and interannual variability

[a]All these experiments are performed for the period of March 2000 to November 2011. See the text of Section 2.2 for details. Note that the forcing fields for the NoSeason experiment contain the climatologic annual-mean values and the 120 day high-pass filtered anomalies.

Pacific Oceans [e.g., *Li et al*., 2013, 2014, 2015]. In this study HYCOM is configured to the tropical and subtropical PO basin (110°E–70°W, 48°S–48°N) with 1/3°×1/3° horizontal resolution. Three 5° sponge layers are applied to the western, southern, and northern open-ocean boundaries, where model temperature and salinity are relaxed to WOA09 climatology [see *Antonov et al*., 2010; *Locarnini et al*., 2010; *Li et al*., 2015, Figure 1b]. The model has 26 vertical layers, and the top layer thickness is ~2.6 m. Realistic bathymetry from the National Geophysical Data Center (NGDC) 2′ digital data are used after a 1.5°×1.5° smoothing. No-slip condition is applied along continental boundaries. The diffusion and mixing parameters are specified in *Li et al*. [2013].

Surface forcing fields include 2 m air temperature and humidity, surface net shortwave radiation (SWR) and longwave radiation (LWR), precipitation, 10 m wind speed, and surface wind stress. Evaporation and turbulent (latent and sensible) heat fluxes are calculated with the model sea surface temperature (SST), wind speed, air temperature, and specific humidity using the Coupled Ocean-Atmosphere Response Experiment (COARE) 3.0 algorithm [*Kara et al*., 2005]. Consequently, evaporation and turbulent heat fluxes in the model include the SST feedback effects. The 2 m air temperature and humidity are from the European Centre for Medium-Range Weather Forecasts (ECMWF) Re-analysis Interim (ERA-Interim) product [*Dee et al*., 2011] with a 0.75° horizontal resolution available since 1979. For surface net SWR and LWR, we use the geostationary enhanced 1° product from Clouds and the Earth's Radiant Energy System (CERES) [*Wielicki et al*., 1996; *Loeb et al*., 2001] for the period of March 2000 to November 2011. The precipitation forcing is taken from the 0.25°×0.25° TRMM TMPA level 3B42 product. The surface winds are from the 0.25°×0.25° CCMP 10 m vector wind data, which are available during July 1987 to December 2011. Zonal and meridional surface wind stress, τ^x and τ^y, are calculated using the standard bulk formulae. Noted that in HYCOM, wind speed and wind stress are separate inputs into the model as surface forcing fields. They affect the ocean through different processes. While wind stress directly drives ocean dynamical processes and vertical entrainment, wind speed affects SSS mainly through evaporation. Such model setting allows us to separately evaluate the effect of wind stress-driven oceanic processes and that of wind speed-controlled evaporation on SSS ISV (see below).

The model is spun-up from a state of rest for 30 years under monthly climatologic atmospheric forcing, using WOA09 climatology as the initial condition. Starting from the already spun-up ocean state, HYCOM is integrated forward using daily atmospheric forcing from March 2000 to November 2011. The starting and ending dates are determined by the availability of CERES radiation data at the time when the model experiments were performed. Six parallel experiments are performed to quantify the effects of different processes (Table 1). The main run (MR) is forced with the original daily forcing. Its solution contains the complete processes, and is therefore used as the reference solution and compared with observations to evaluate the model performance. In the NoMJO experiment, all the forcing effects of MJOs are removed by low-pass filtering the forcing fields with a 105 day Lanczos digital filter [*Duchon*, 1979]. In this study we do not distinguish the MJOs from other types of atmospheric intraseasonal oscillations, such as convectively coupled intraseasonal Kelvin and Rossby waves [e.g., *Wheeler and Kiladis*, 1999; *Kiladis et al*., 2009]. Given that the MJO is the most influential intraseasonal mode in the western tropical PO [e.g., *Zhang*, 2005], here we use the "MJO effect" to represent the total effect of atmospheric intraseasonal variability on the ocean. Without intraseasonal atmospheric forcing, SSS ISV in NoMJO arises only from the ocean internal processes [e.g., *Jochum and Murtugudde*, 2005; *Zhou et al*., 2008]. The solution difference, MR – NoMJO, measures the overall MJO forcing effect on the ocean.

In the NoP experiment, precipitation is low-pass filtered at the 105 day period, and the other forcing fields are the same as in MR. The difference, MR – NoP, isolates the intraseasonal precipitation effect. In NoWND, the wind forcing, including both wind speed and wind stress, is 105 day low-pass filtered, and MR – NoWND measures the total wind forcing effect on the ocean. In the NoTAU experiment, only wind stress is low-pass

filtered. The difference, MR – NoTAU, quantifies the MJO wind stress effect through oceanic processes (e.g., horizontal advection, upwelling and entrainment). On the other hand, NoTAU – NoWND, measures the MJO wind speed effect through evaporation.

The above five experiments are identical to those described in *Li et al*. [2015]. *Li et al*. [2015] also discussed a NoSWR experiment, in which SWR is low-pass filtered to assess the effect of intraseasonal SWR on SSS through changing SST and thus evaporation. This effect, however, is much smaller than effects of precipitation and winds. Thus no further discussion for SWR effect is provided in this study. To explore the seasonality of SSS ISV, we perform another experiment. Two major factors determine the amplitude of SSS ISV: the strength of the MJO forcing and the ocean background state (such as surface mixed layer thickness). Both undergo prominent seasonal variations and therefore induce seasonal variations of the SSS ISV amplitude. To examine the relative importance of the two factors, we perform a no-seasonality (NoSeason) experiment, in which all the forcing fields are 120 day high-pass filtered anomalies (intraseasonal fluctuations) plus the annual-mean climatology of 2000–2011. In this experiment, the seasonal and interannual variations in the forcing fields are removed. Therefore, the seasonality of SSS ISV in NoSeason is predominantly caused by the seasonality of the MJO, and that in the MR – NoSeason is caused by seasonal variation of the oceanic background state. Some seasonal oceanic variations may arise from the rectification of MJOs [e.g., *Duncan and Han*, 2012] and ocean internal instability, which are still contained in the NoSeason experiment. These variations are expected to be much smaller than those induced by seasonal external forcing and will not significantly affect our results.

Output data from all the experiments are stored in 3 day-mean resolution for the period of March 2000 to November 2011. To suppress the transient effect from the spin-up, the output data in 2000 and 2001 are discarded. The 10 year data of 2002–2011 are used for our analysis. We analyze the 20–90 day band-pass filtered anomalies to explore SSS ISV. To remove the ending-point effect of the filter, we discard 45 days of data from the beginning and the end of the data time series.

3. Results

3.1. HYCOM Performance in the Western Tropical PO

Li et al. [2015] provided a detailed comparison between HYCOM MR solution and observations (both satellite and in-situ) and demonstrated that HYCOM is able to realistically simulate the mean state and intraseasonal variability of the tropical Indo-Pacific Ocean (their Figures 2–8). Here we provide further validations but only for the western tropical PO. Figure 1b shows the STD of 20–90 day SSS from HYCOM MR. Its overall structure is consistent with Aquarius observation (Figure 1a). The simulated ISV STD is weaker than Aquarius data by 0.02–0.03 psu, accounting for ∼20% of the total ISV. One major cause of the underestimation is likely the difference in SSS definition. While HYCOM SSS is the bulk salinity value of the top 2.6 m (thickness of the top model layer), Aquarius SSS is the top-centimeter ocean salinity, which is more sensitive to surface forcing. HYCOM-simulated SSS ISV is evidently weaker in the region north of 15°N, which may be due to the underrepresentation of the strong mesoscale eddy variability there [e.g., *Qiu*, 1999] in our 1/3°-resolution simulation. The STD of 20–90 day SSS in Aquarius CAP-RC data (Figure 1c) is generally smaller than that of Aquarius CAP data. Their difference reaches as large as 0.02–0.05 psu in the western tropical PO (Figure 1d), accounting for 10–30% of the total SSS ISV in CAP data. The rain-induced uncertainty is likely a considerable issue for the Aquarius-measured SSS ISV in the heavy-rainfall western tropical PO region.

Albeit with some quantitative discrepancies, the leading two EOF modes of MR 20–90 day SSS (Figures 2c and 2d) exhibit similar spatial patterns to those of Aquarius SSS. To explore the ISV characteristics in different areas, we define four boxes based on the spatial patterns of the two EOFs. The western box covers the far western equatorial PO (140°E–155°E, 2.5°S–2.5°N); the eastern box covers the eastern part of the western equatorial PO (155°E–170°E, 2.5°S–2.5°N); the northern and southern boxes represent the northeastern tropical PO (135°E–150°E, 3°N–8°N) and southwestern tropical PO (160°E–175°E, 9°S–4°S). Figure 3 shows the 20–90 day SSS from HYCOM MR and Aquarius CAP data averaged over the four boxes. Since we have discarded 45 days from the beginning and end of the band-pass filtered data, there is little overlapping between Aquarius and HYCOM. Consistent with Figure 1, the HYCOM-simulated SSS ISV is weaker than Aquarius observation by ∼20% as measured by STD values. For both the Aquarius and HYCOM data, the amplitude of SSS ISV shows evident seasonal variation. This aspect will be discussed in section 3.3.

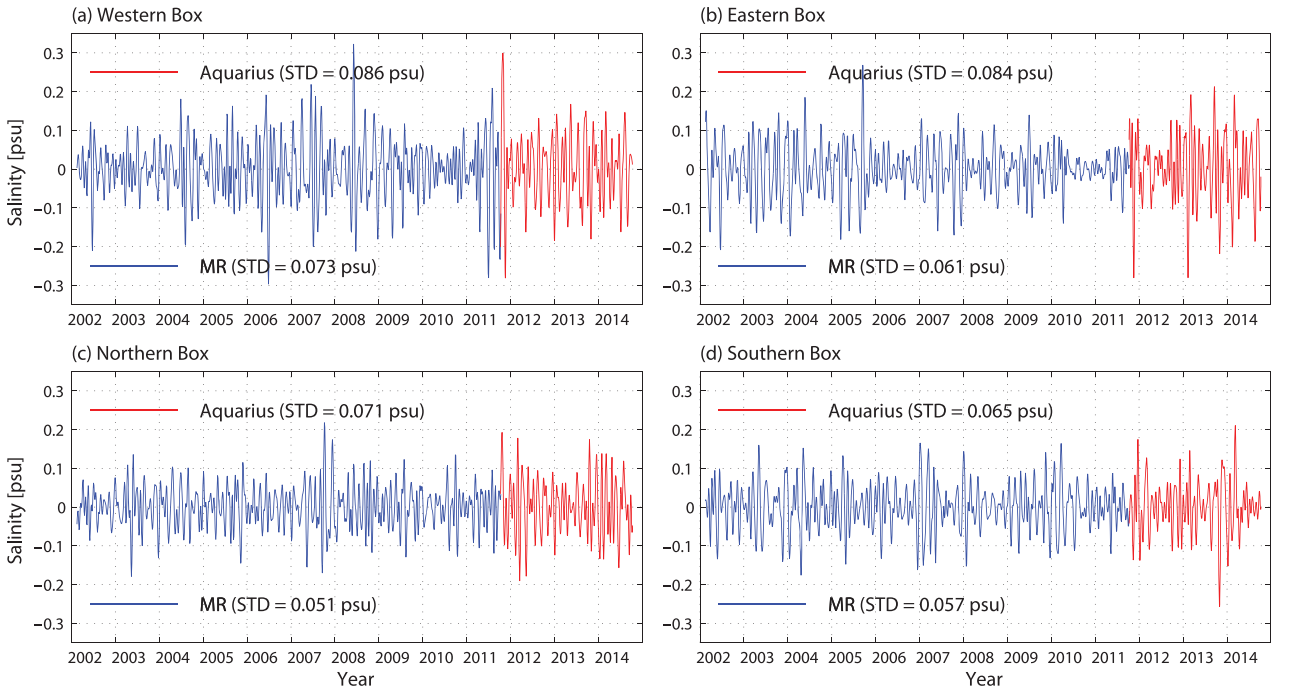

Figure 3. Time series of the 20–90 day SSS from Aquarius CAP data (red) and HYCOM MR (blue) averaged over the (a) the western box, (b) the eastern box, (c) the northern box, and (d) the southern box. See Figure 2 for the boxed regions.

The surface mixed layer depth (MLD) is a key factor for the amplitude of SSS ISV. A thinner mixed layer favors stronger salinity variability in response to various forcing processes. The MLD in the western tropical PO undergoes prominent seasonal variation (Figures 4a–4d). Here the MLD is defined as the depth at which the potential density increase $\Delta\sigma$ from the 10 m value is equivalent to temperature decrease by $\Delta T = 0.5°C$ [*de Boyer Montégut et al*., 2004],

$$\Delta\sigma = \sigma(T_{10} - \Delta T,\ S_{10},\ P_{10}) - \sigma(T_{10},\ S_{10},\ P_{10}), \tag{1}$$

where T_{10}, S_{10}, and P_{10} are temperature, salinity, and pressure at 10 m, respectively. In boreal winter (December, January, and February; DJF), the MLD is thick (thin) in the northern (southern) hemisphere due to reduced (increased) surface heat flux. The pattern is reversed in boreal summer (June, July, and August; JJA), as the solar heating center moves to the southern hemisphere. Such seasonal transition is well reproduced by HYCOM MR. Comparing with the observed MLD, the HYCOM-simulated MLD is thicker by ~10 m in the high-STD region of the western tropical PO in both seasons. This could be another reason for the underestimated SSS ISV in HYCOM (Figures 1 and 3).

Since ocean advection is potentially important in causing SSS ISV, it is necessary to further examine the HYCOM-simulated surface ocean current and its seasonality. The OSCAR current is an estimate of 0–30 m ocean current based on satellite observations [*Bonjean and Lagerloef*, 2002] (Figures 4e and 4g). Here we also compute the mean U of the top 30 m of MR to obtain a fair comparison (Figures 4f and 4h). The structures of the major currents, such as the westward flowing North Equatorial Current (NEC) between 8°N and 17°N, the eastward North Equatorial Countercurrent (NECC) at 2°N–7°N, and the westward South Equatorial Current (SEC) near the equator, are all well represented in MR, except that the westward flows are stronger in HYCOM. Primary features of the seasonal variation in the western tropical PO circulation include the strengthening of the NEC and weakening of the NECC in boreal winter [e.g., *Johnson et al*., 2002; *Yaremchuk and Qu*, 2004], the southward shift of the NECC in boreal summer [*Hsin and Qiu*, 2012], the appearance of the eastward South Equatorial Countercurrent in boreal winter (at ~10°S) [*Gouriou and Toole*, 1993], and the seasonal reversal of the New Guinea Coast Current (NGCC) northeast of the New Guinea island [e.g., *Lindstrom et al*., 1987; *Kuroda*, 2000; *Ueki et al*., 2003]. These features are faithfully reproduced by HYCOM. We have also compared the ISV of surface current (figures not shown). The 20–90 day U in MR compares favorably with OSCAR data [see *Li et al*., 2015, Figure 7], indicating that HYCOM is capable of realistically represent the horizontal advection process associated with intraseasonal SSS variability.

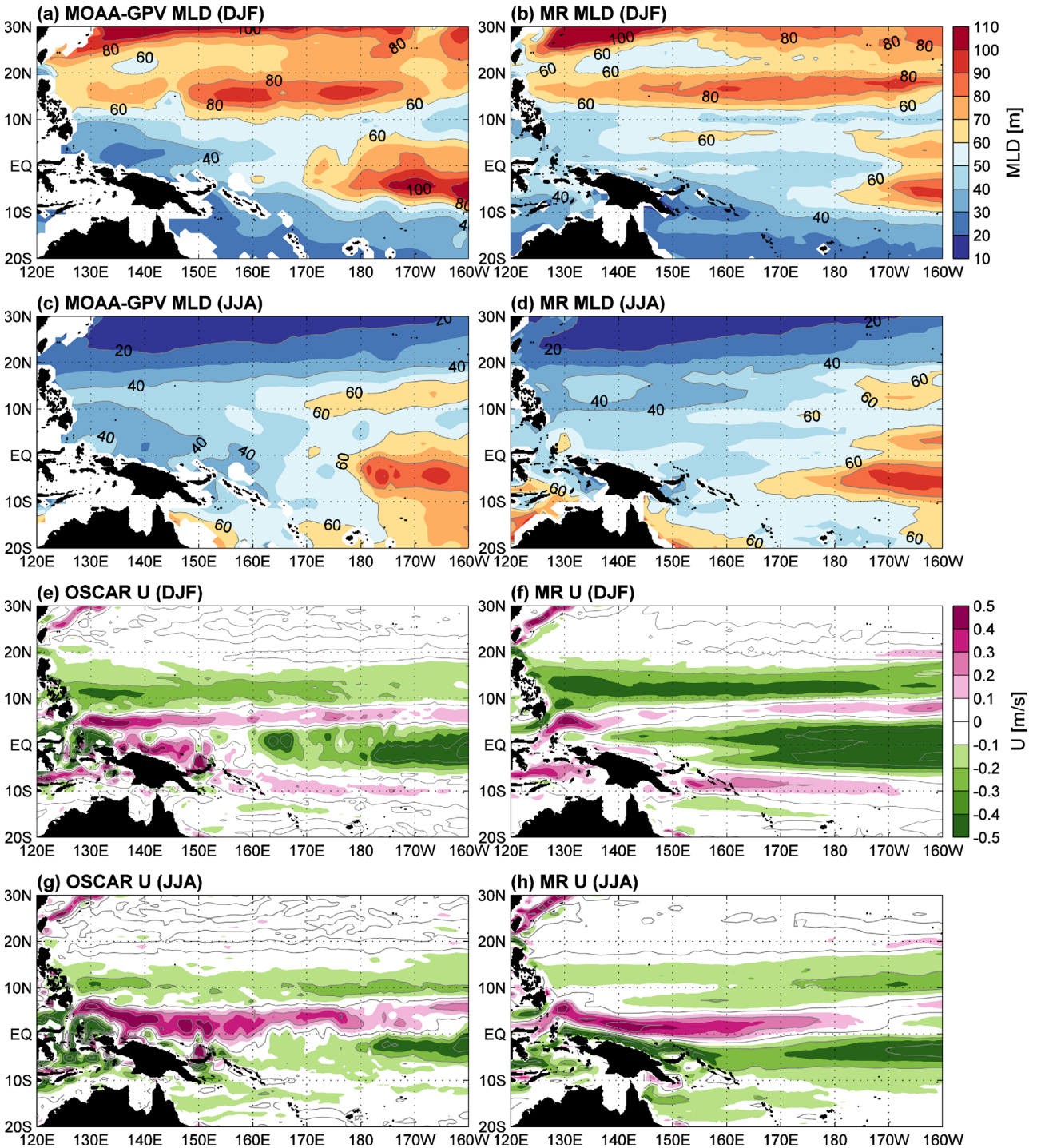

Figure 4. Compare the climatologic DJF MLD (m) from (a) MOAA-GPV data and (b) HYCOM MR for 2002–2011, while (c) and (d) compare the JJA MLD maps. (e–h) Same as Figures 4a–4d but for the surface-layer U (m s^{-1}) from OSCAR data and HYCOM MR averaged in the top 30 m.

3.2. Mechanisms of SSS ISV

STD of the 20–90 day SSS from MR, representing the total modeled SSS ISV, is largest in the western box and smallest in the northern box (Table 2). As discussed in section 2.2, the "MJO effect" can be measured by MR – NoMJO, which refers to the total forcing effect by atmospheric intraseasonal variability that is dominated by the MJO. The STDs of SSS ISV produced by MJO forcing are 0.074, 0.061, 0.053, and 0.055 psu in

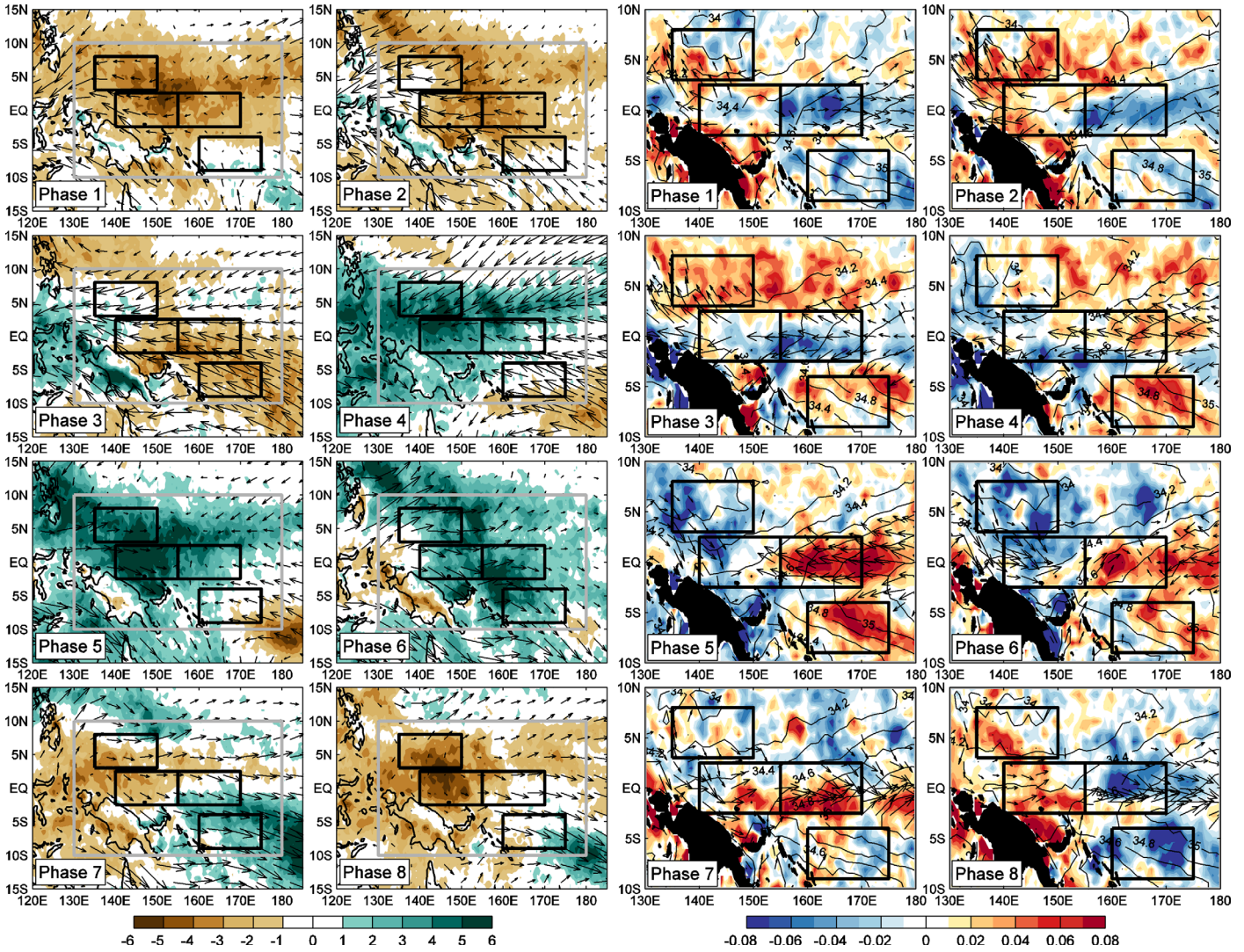

Figure 5. Left two columns show MJO composite maps of the 20–90 day CCMP wind stress (vectors) and 20–90 day TRMM precipitation (color shading; in 10^{-8} m s^{-1}), while right two columns show MJO composite maps of 20–90 day SSS (color shading; in psu), 20–90 day surface current (vector), and the unfiltered SSS (black contours; in psu; with 0.2 psu intervals) from HYCOM MR. Surface currents smaller than 0.04 cm s^{-1} are not plotted. MJO composites are based on the RMM index. Note that right columns are for only for the high-STD region (indicated by the grey rectangle in the left columns).

the western, eastern, northern and southern boxes, respectively, which are very close to the STD values from MR (Table 2). The correlations between MR and MR – NoMJO are between 0.82 and 0.93 for the four boxes (Table 2). These results demonstrate that most of the SSS ISV in the western tropical PO is forced by atmospheric intraseasonal variability. As a comparison, the effect of ocean internal (unforced) variability is apparently smaller, with STDs of 0.020–0.037 psu. Its relative magnitude to the total ISV STD is largest in the northern box (∼58%) and smallest in the southern box (∼35%). Its correlation with the total ISV is quite low, ranging between 0.02 and 0.10. It is likely that ocean internal processes can induce considerable SSS variations, but these variations do not constructively contribute to the total SSS ISV signals dominated by atmospheric forcing effect.

Passage of a MJO event involves multivariate atmospheric fluctuations at the sea surface. Among others, precipitation, wind stress, and wind speed are important in causing SSS variability. Below, we quantify each effect using the hierarchy of HYCOM experiments described in section 2.2. Overall, effects of wind stress-driven oceanic processes and precipitation have much higher correlation with the total SSS ISV than the effect of wind speed-induced evaporation, with correlation coefficients ranging from 0.42 in the northern box to 0.70 in the eastern box (> 95% significance) for wind stress, and from 0.34 in the eastern box to 0.56

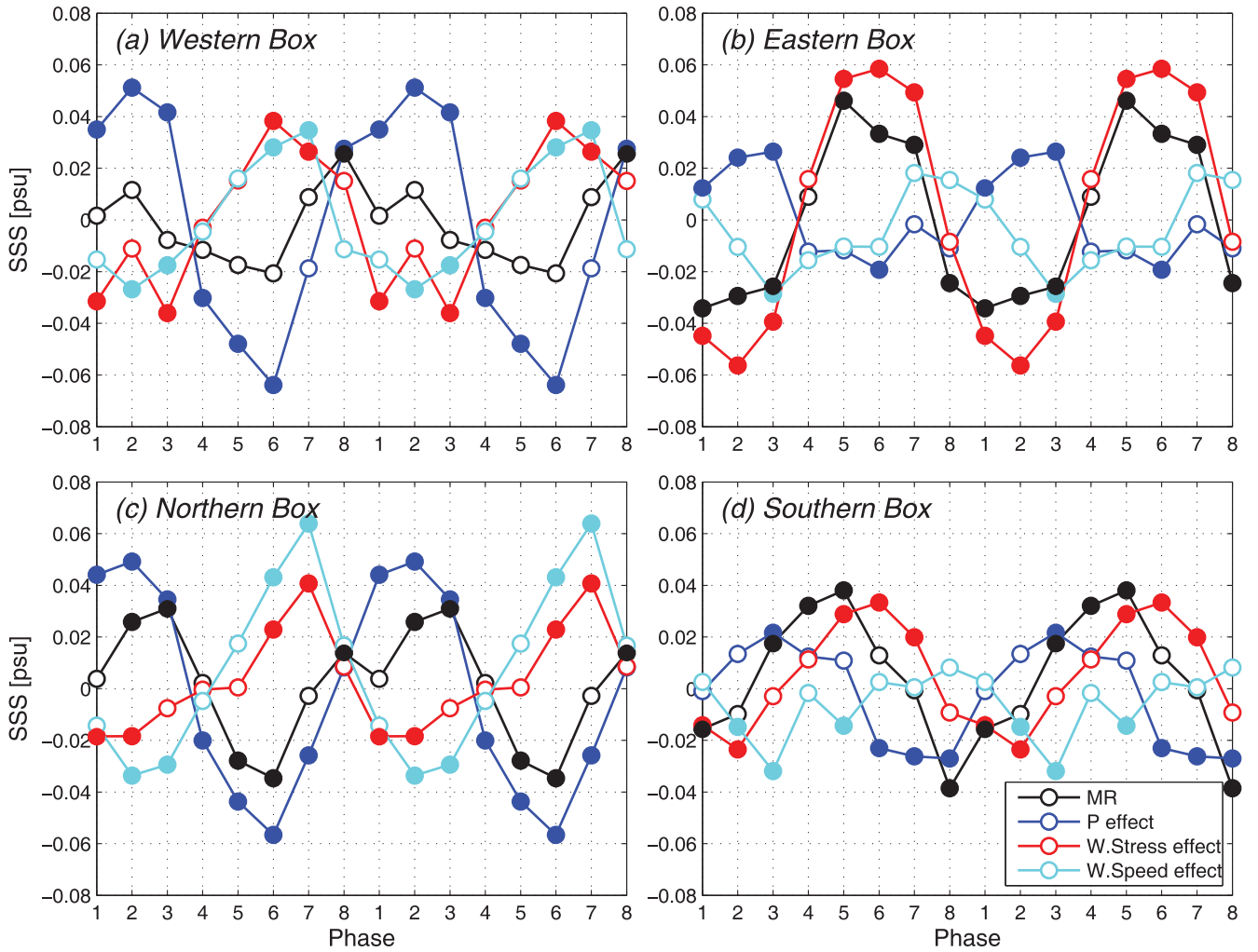

Figure 6. MJO composites of 20–90 day SSS from HYCOM MR (black), precipitation effect (blue; MR – NoP solution), wind stress effect (red; MR – NoTAU), and wind speed effect (cyan; NoTAU – NoWND) averaged for the (a) western box, (b) eastern box, (c) northern box, and (d) southern box. MJO composites are based on the RMM index (see Figure 5). Composite values above (below) 95% confidence level are shown by the curves with solid (blank) circles, determined by a two-tailed students' *t*-test.

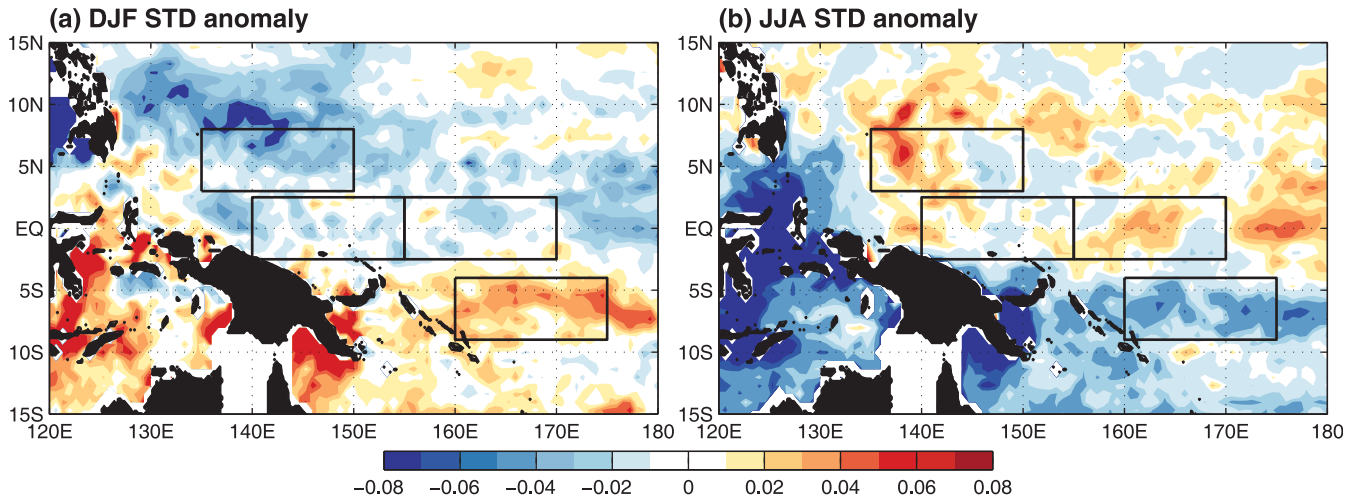

Figure 7. (a) Anomaly of 20–90 day SSS STD for DJF relative to the all-season STD of 20–90 day SSS (in psu) from HYCOM MR during 2002–2011. (b) Same as Figure 7a but for the JJA STD anomaly.

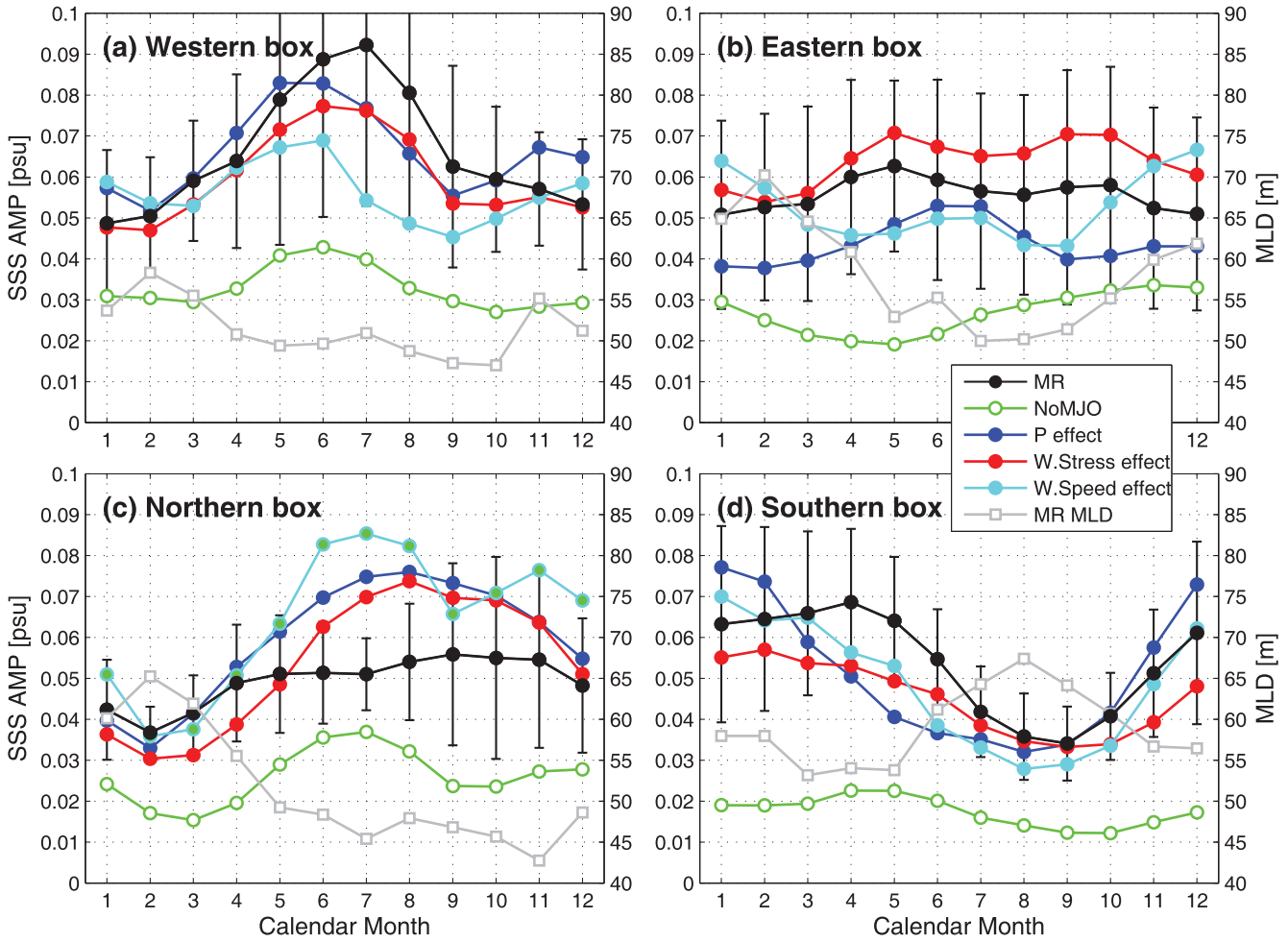

Figure 8. Seasonal cycle of the amplitude of SSS ISV (AMP) from MR (black), NoMJO (green), precipitation effect (blue; MR – NoP solution), wind stress effect (red; MR – NoTAU solution), and wind speed effect (green; NoTAU – NoWND solution) in the (a) western box, (b) eastern box, (c) northern box, and (d) southern box. The grey curves denote MLD from MR solution. Black bars denote the one STD range of the MR SSS AMP.

in the southern box for precipitation (Table 2). In contrast, the effect of wind speed is negatively correlated with the total SSS ISV in all boxes, with the maximum value being −0.26 in the southern box. The STD magnitudes, however, are comparable for all three effects (Table 2). These results indicate that evaporation induced by wind speed change generally damps the SSS signals produced by precipitation and wind stress forcing. The relative importance of precipitation and wind stress-driven oceanic processes varies among the four areas. In the eastern box, wind stress dominates precipitation in causing SSS ISV, with STD being 0.069 psu and correlation being 0.70 comparing to 0.047 psu and 0.34 for precipitation. This result agrees with *Li*

Table 2. STD values of 20–90 Day SSS (psu) From Different Processes in the Four Regions[a]

Process (solution)	Western Box	Eastern Box	Northern Box	Southern Box
Total SSS (MR)	0.073 psu	0.061 psu	0.051 psu	0.058 psu
MJO forcing (MR - NoMJO)	0.074 psu (***r*=0.86***)	0.061 psu (***r*=0.86***)	0.053 psu (***r*=0.82***)	0.055 psu (***r*=0.93***)
Ocean internal variability (NoMJO)	0.037 psu (r=0.08)	0.031 psu (r=0.09)	0.030 psu (r=0.10)	0.020 psu (r=0.02)
Precipitation effect (MR - NoP)	0.071 psu (***r*=0.54***)	0.047 psu (***r*=0.34***)	0.065 psu (***r*=0.38***)	0.056 psu (***r*=0.56***)
W. Stress effect (MR - NoTAU)	0.065 psu (***r*=0.64***)	0.069 psu (***r*=0.70***)	0.061 psu (***r*=0.42***)	0.049 psu (***r*=0.57***)
W. Speed effect (NoTAU - NoWND)	0.064 psu (r=−0.10)	0.064 psu (r=−0.07)	0.060 psu (r=−0.10)	0.055 psu (***r*=−0.26***)

[a]Their correlation coefficients with the MR 20–90 day SSS are shown in the brackets, and those significant at 95% confidence level are written bold and marked with asterisks.

et al. [2015], given that our eastern box largely overlies their "western PO box" (155°E–165°E, 5°S–5°N). In the western, northern and southern boxes, the two effects are comparable, with precipitation effect having somewhat larger STDs and wind stress effect having higher correlations.

To further understand the relationship between different processes, we conduct a composite MJO analysis based on the real-time multivariate MJO (RMM) index [*Wheeler and Hendon*, 2004]. The RMM index is based on the first two EOFs of the combined fields of near-equatorial 850 hPa and 200 hPa winds and the outgoing longwave radiation from observational and reanalysis data. Projecting atmospheric fields onto the two EOFs yields two principal components, defined as the RMM time series 1 (RMM1) and RMM time series 2 (RMM2). Here we use the phase (varying between 1 and 8) and magnitude $(RMM1^2 + RMM2^2)^{1/2}$ of the RMM index for our composite. For each of the eight MJO phases, the 20–90 day band-pass filtered variables over the days with RMM magnitude > 1.5 (indicating large atmospheric perturbations associated with the MJO) are averaged. Left two columns of Figure 5 display the precipitation and wind stress anomalies at each phase of the composite MJO during 2002–2011. Phase 1 is characterized by suppressed precipitation in the western tropical PO with the dry-condition center at $\sim$150°E along the equator. Suppressed convection is accompanied with surface wind divergence, with easterly winds to the west and westerly winds to the east of the dry-condition center. The negative precipitation anomalies gradually decay and spread to the off-equatorial regions from Phase 2 to Phase 3, during which strong easterly winds prevail. Enhanced precipitation anomalies occupy the equatorial region in Phase 4 accompanied by surface wind convergence, as indicated by the southwesterly (northwesterly) winds to the northeast (southeast) of the precipitation center. Variations of precipitation and surface winds during Phases 5–8 are basically opposite to those during Phases 1–4, with similar spatial structures but a reversed sign.

In comparison, SSS variations from HYCOM MR during the composite MJO phases (right two columns of Figure 5) exhibit much more complicated spatial structures than those of precipitation and winds. Note that SSS anomaly map is shown only for the high-STD region of Figure 1. Even though precipitation is not a dominant process in any of the four areas (Table 2), signatures of MJO precipitation on SSS can be identified in some areas. For example, the dry condition during Phases 8–3 corresponds to positive SSS anomalies in the northern box during phases 8–3 and southern box during phases 3 and 4. Similarly, the enhanced MJO precipitation during Phases 4-6 corresponds to negative SSS anomalies in the western and northern boxes. In the eastern box, however, precipitation signatures are not evident, because the SSS anomalies in this region are dominated by wind-driven oceanic processes as discussed above. The prevailing westerly winds during Phases 6–8 lead to eastward currents along the equator during Phases 7–1, which transport fresher water from the west and produce negative SSS anomalies in the eastern box during Phases 8–3. Likewise, easterly winds during Phases 2–4 lead to westward flows along the equator during Phases 3–5, producing positive SSS anomalies during Phases 4–7 by bringing saltier water from the central PO to the eastern box. In addition, anomalous meridional Ekman advection induced by zonal wind anomalies can affect SSS variations in the off-equatorial regions. For example, equatorial easterly winds during Phases 2–4 induce meridional current divergence particularly in the western box, which contributes to the positive SSS anomalies in off-equatorial areas by carrying higher-salinity water poleward. Consistent with Table 2, these composite maps suggest that the MJO causes SSS variations through both precipitation and wind stress-driven ocean current advection, and the latter is particular important in the eastern box.

We further assess the effects of precipitation, wind stress, and wind speed during the evolution of the composite MJO for each box (Figure 6). The composite cycles are plotted twice to better visualize the evolution from Phase 8 to Phase 1. In the western box (Figure 6a), the precipitation effect has the largest amplitude but it is out of phase with the wind stress and wind speed effects. The latter two are in phase. The offsetting between precipitation and wind effects leads to weak total SSS anomaly (black), and only the maximum of the total SSS anomaly during Phase 8 is statistically significant at 95% confidence level. The negative SSS anomalies during Phases 4–6 are mainly produced by precipitation, and their magnitudes are greatly reduced by the effect of winds. By contrast, in the eastern box (Figure 6b), the total SSS anomalies are dominated by wind stress effect. Effects of precipitation and wind speed generally acts to attenuate the total SSS anomaly, although wind speed effect contributes to the positive SSS anomaly in Phase 7 and the negative one in Phase 3. The situation is reversed in the northern box (Figure 6c), where precipitation effect is most important in producing SSS anomalies, while the total effect of winds acts to attenuate SSS anomalies produced by precipitation. In the southern box (Figure 6d), the total SSS anomalies are contributed from both

Table 3. STD Values of 20–90 Day Mixed Layer Salinity Tendency $\partial[S]/\partial t$, Salinity Advection Term ADV, and Vertical Entrainment ENT Calculated With MR Output[a]

Process	Western Box	Eastern Box	Northern Box	Southern Box
$\partial[S]/\partial t$	0.0091 psu/d	0.0074 psu/d	0.0065 psu/d	0.0071 psu/d
ADV	0.0044 psu/d (***r*=0.49***)	0.0063 psu/d (***r*=0.69***)	0.0032 psu/d (***r*=0.31***)	0.0068 psu/d (***r*=0.67***)
ENT	0.0036 psu/d (***r*=0.64***)	0.0029 psu/d (***r*=0.61***)	0.0025 psu/d (r=0.19)	0.0025 psu/d (r=0.16)

[a]Correlation coefficients with $\partial[S]/\partial t$ are shown in the brackets, and those significant at 95% confidence level are written bold and marked with asterisks.

wind stress and precipitation effects, leading precipitation effect by one phase and lagging wind stress effect by one phase. Wind speed effect is relatively small here.

In summary, results from Table 2 and Figure 6 suggest that precipitation and wind stress are the two major drivers of SSS ISV in the western tropical PO. Their relative importance shows significant spatial variations. While wind stress-induced oceanic processes are the dominant forcing for the equatorial PO east of 155°E, precipitation produces larger SSS anomalies in the northwestern tropical PO. In the far western equatorial PO and southwestern tropical PO, they are of roughly equal importance. It should be noted that due to the complex interaction among different processes, the sum of each effect does not exactly equal to the total SSS ISV.

Wind stress effect on mixed layer salinity is mainly through horizontal advection and vertical entrainment. *Li et al.* [2015] evaluated their relative contributions for 155°E–165°E, 5°S–5°N region and found that horizontal advection is more important than vertical entrainment. Here we compute the two terms together with the mixed layer salinity tendency $\partial[S]/\partial t$ with MR output but for each of the four regions. Here bracket [•] denotes the mean value of the surface mixed layer. Mixed layer advection (ADV) can be calculated as

$$\mathrm{ADV} = -[\mathbf{u} \cdot \nabla S], \tag{2}$$

where $\mathbf{u} = (u, v)$ is the horizontal current vector, and $\nabla S = (\partial S/\partial x, \partial S/\partial y)$ is the horizontal gradient of salinity.

Vertical entrainment term ENT is calculated as [*Stevenson and Niiler*, 1983],

$$\mathrm{ENT} = -\frac{[S]-S_{-H}}{H} \times \left(w_{-H} + \frac{\partial H}{\partial t} + \mathbf{u}_{-H} \cdot \nabla H\right), \tag{3}$$

where S_{-H} and w_{-H} are the salinity value and vertical velocity at the mixed layer base, $\partial H/\partial t$ is the local MLD tendency, and $\mathbf{u}_{-H} \cdot \nabla H$ is the MLD change induced by horizontal advection. The STDs of the 20–90 day ADV, ENT, and $\partial[S]/\partial t$ averaged in each of the four boxes are summarized in Table 3. While ADV has a significant correlation with $\partial[S]/\partial t$ in all the four areas, ENT is significant only in the western and eastern boxes. ADV contribution is much larger than ENT in the eastern and southern boxes, where its magnitude accounts for ~90% of $\partial[S]/\partial t$, and its correlation with $\partial[S]/\partial t$ is high (0.75 and 0.69). In the western and northern boxes, ADV magnitude is below 50% of $\partial[S]/\partial t$ and only slightly larger than ENT. Given that wind stress effect on SSS ISV is more important in the eastern and southern boxes (Figure 6), we conclude that in the western tropical PO wind stress effect on SSS ISV is primarily through ocean current advection, and to a lesser degree through vertical entrainment, similar to the situation in the equatorial Indian Ocean [*Li et al.*, 2015].

3.3. Seasonality of SSS ISV

The western tropical PO is subjected to strong influence of the East Asian Monsoon. Seasonal variation of the ocean state can modulate the ocean response to MJO forcing. In addition, the amplitude, structure, and propagation behaviors of the MJO also exhibit evident seasonality [e.g., *Zhang*, 2005], which can also leave to the seasonality of SSS ISV. Figure 7 shows the seasonal anomaly of STD of 20–90 day SSS in DJF and JJA, i.e., the deviation of STD value in a season from the all-season STD value. In DJF SSS ISV is reduced in the northern hemisphere and enhanced in the southern hemisphere (Figure 7a), and the pattern is reversed in JJA (Figure 7b). Aquarius SSS data during 2011–2014 show basically similar seasonal transition but with many small-scale structures, which reflect mesoscale eddies that cannot be averaged out with the 3 year Aquarius records (figures not shown). The seasonal variation of SSS ISV in Figure 7 reminisces that of MLD in

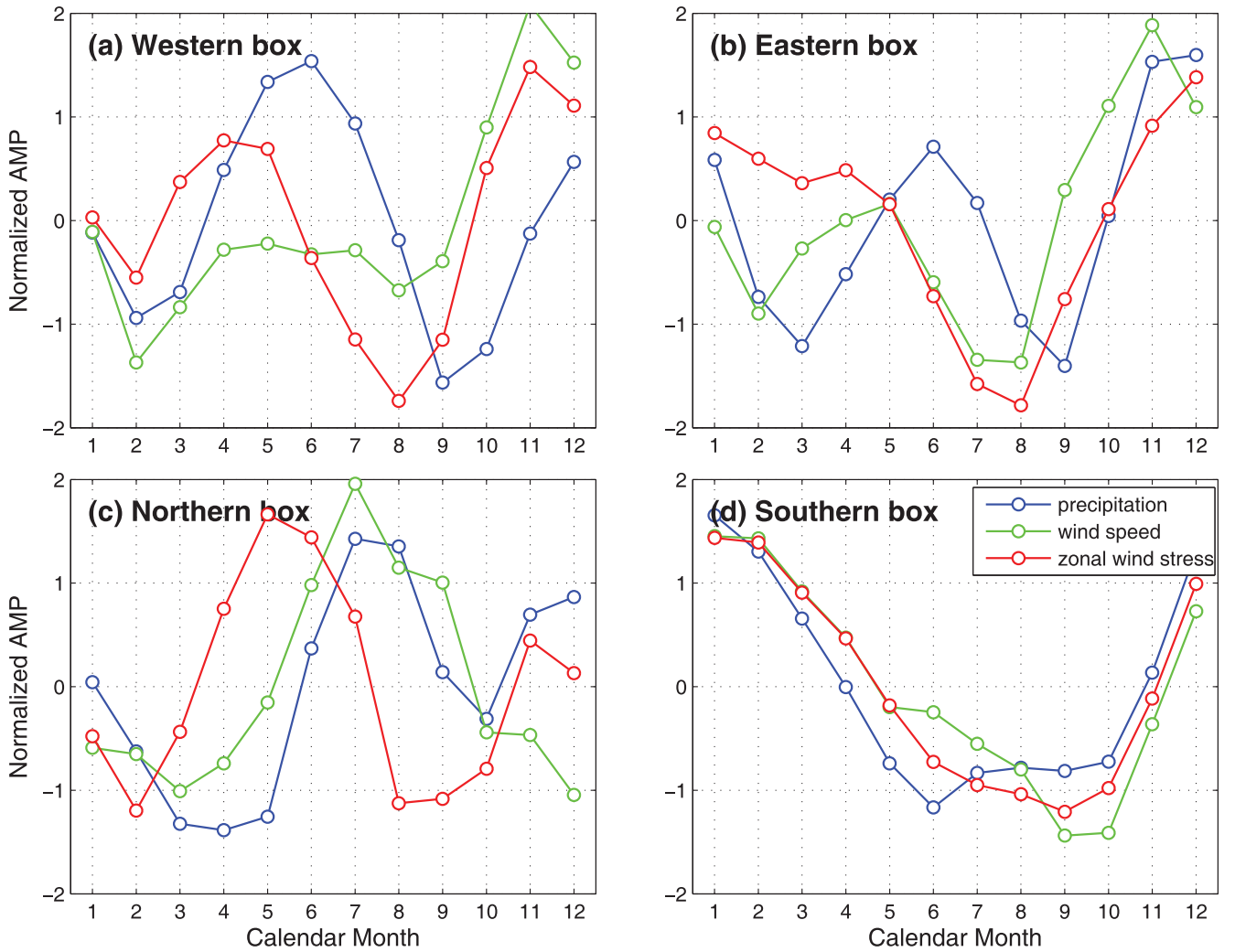

Figure 9. Seasonal cycles of AMP of precipitation (blue), wind speed (green), and zonal wind stress (red). All variables are shown as normalized anomalies to achieve better comparison.

Figures 4a–4d. Deeper (shallower) MLD in the northwestern tropical PO in DJF (JJA) leads to weaker (stronger) SSS responses to various forcing processes. Likewise, local MLD change can also well explain the seasonality of SSS ISV in the southwestern tropical PO. MLD is likely an important factor regulating the seasonality of SSS ISV amplitude.

The amplitude (AMP) of SSS ISV can be quantified by the moving-window STD of the 20–90 day SSS,

$$\mathrm{AMP}\ (t)=\sqrt{<[\mathrm{SSS}^{20-90}(t-60:t+60)]^2>/n}, \tag{4}$$

where $\mathrm{SSS}^{20-90}(t-60: t+60)$ is the 20–90 day SSS anomaly time series within the 121 day window between t - 60 day and $t+60$ day, $<\bullet>$ denotes summation, and $n=41$ is the data sample number within the 121 day window. AMP can be computed for 20–90 day SSS from MR and from other solutions that isolate different processes (Figure 8). The seasonal variation of AMP from MR (black) is large in the western and southern boxes with a seasonal difference of 0.03–0.04 psu, which exceeds 50% of the annual-mean AMP value. AMP variation is relatively weaker in the northern box with a 0.02 psu seasonal difference and is the weakest in the eastern box where the seasonal cycle is within one standard deviation range.

In the western box (Figure 8a), SSS ISV is enhanced during May–August and weakened during December–February. Such seasonal variation can be caused by both the seasonality of MJO forcing (precipitation, wind stress, and wind speed) and that of the ocean state. During May–August MLD (grey line; scaled by the right axis) is thinner than the winter value by ~5 m, which might be one of the causes for the seasonal difference

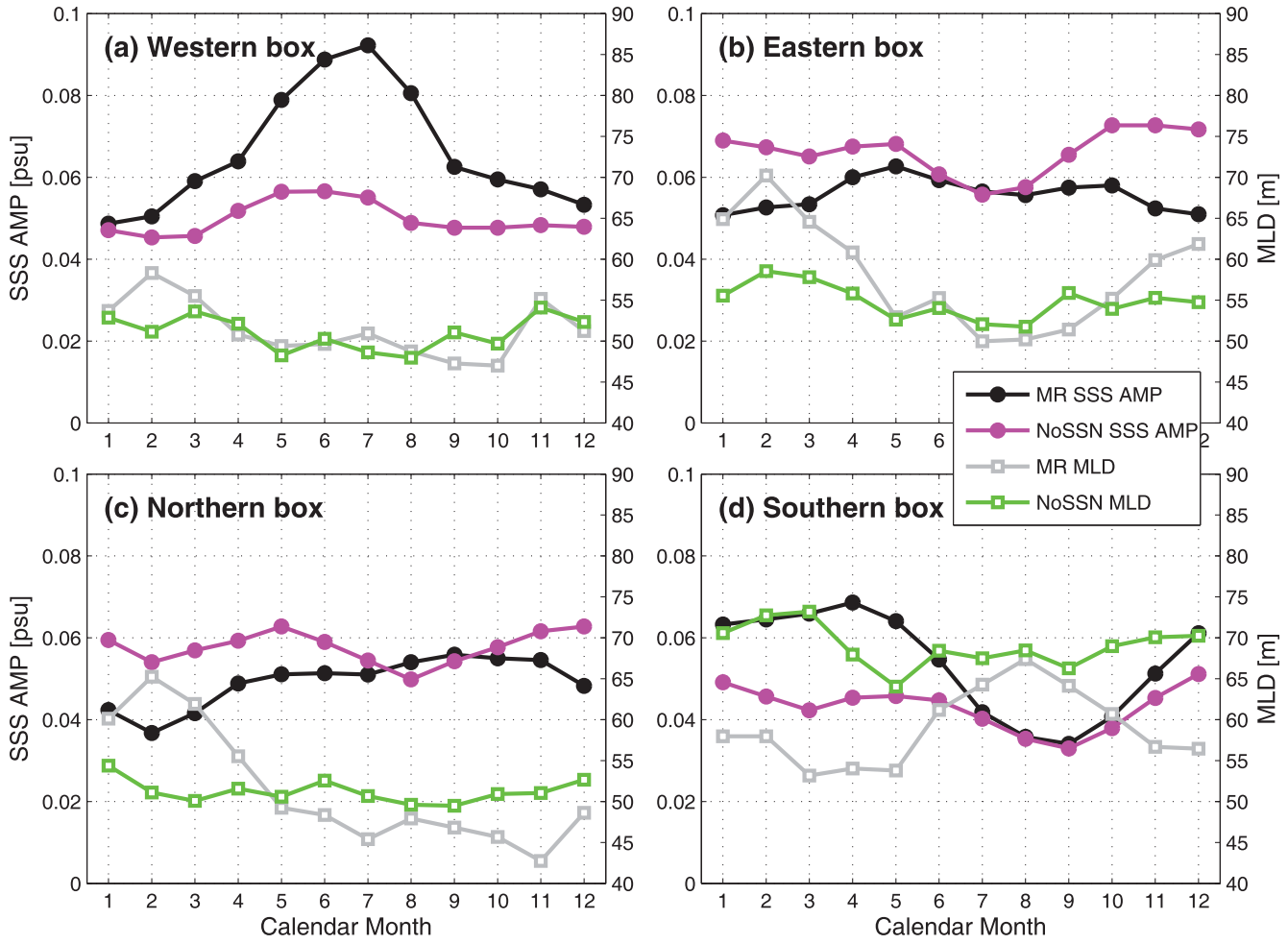

Figure 10. Seasonal cycles of SSS AMP from MR solution (black) and NoSeason solution (pink). Grey (green) curves denote the MLD from MR (NoSeason) solution.

in SSS ISV. Checking the AMPs of forcing fields suggests that ISV of local precipitation is enhanced during summer months (Figure 9a), which may serve as another cause. Seasonal variation of MLD is much larger in the other three areas and able to explain the SSS AMP seasonal cycle by a larger extent. In the eastern box (Figure 8b), the thick MLD from December through March reduces AMP of total SSS, which is dominated by wind stress effect (red). In the northern box (Figure 8c), large MLD during January–March also leads to small AMP of total SSS. In the southern box (Figure 8d), MLD is thick (64–67 m) during July–September and thin ($<$ 55 m) during March–May, which is consistent with the variation in AMP of total SSS. Note that the impact of MLD is not only on AMP of the total SSS but also on all the processes. On the other hand, ISVs of precipitation and winds have strong seasonal variations (e.g., enhancement in boreal winter and reduction in boreal summer in the southern box), which can also contribute to the seasonality of SSS ISV.

To separate the effects of seasonal variations of MJO forcing and the ocean state, we compute AMP of SSS of the NoSeason experiment in which most of the seasonal ocean variations are removed, and seasonality of SSS ISV arises primarily from the seasonality of MJO strength. Figure 10 compares the SSS AMP seasonal cycles from MR (black) and NoSeason (pink). In all the four areas, AMP seasonal cycle of NoSeason is different from that of MR, especially in the western and southern boxes. In these two boxes (Figures 10a and 10d), AMP seasonal cycle of NoSeason is similar in shape to that of MR, but its amplitude is much smaller. In the eastern and northern boxes (Figures 10b and 10c), AMP exhibits weak semiannual variations, mimicking AMPs of precipitation and winds (Figures 9b and 9c). The large difference between MR and NoSeason suggests that seasonal variation of the ocean state is more important in regulating the seasonality of SSS ISV than the strength of MJO forcing, particularly in the western and southern boxes. In the eastern and northern boxes, the seasonality of SSS ISV is weaker and both factors have significant contributions.

The impact of the ocean state is largely through MLD changes, which is obvious in the eastern, northern, and southern boxes. AMP difference between MR and NoSeason can be well explained by MLD. Thinner (thicker) MLD always leads to an increase (decrease) in SSS AMP in MR. However, this relationship does not seem to work well for the western box (Figure 10a). AMP of NoSeason is smaller than that of MR in all seasons. Particularly, the huge difference during May–August is not likely due to MLD, given the small MLD difference between MR and NoSeason. Note that there are still some month-to-month changes in MLD in NoSeason (green), which arise from ocean internal variability and rectification from MJOs [e.g., *Duncan and Han*, 2012]. The enhancement of SSS ISV during these months may be induced by other ocean variations besides MLD or the interaction between the ocean state and atmospheric forcing. One possible explanation is that some of SSS ISV is generated out of the western box and thus not influenced by local MLD changes. The major ocean currents around this area, such as the eastward NECC and the northwestward NGCC, are all strengthened during boreal summer [e.g., *Kuroda*, 2000; *Johnson et al*., 2002; *Yaremchuk and Qu*, 2004] (see also Figure 4). They can transport SSS anomalies from other areas to the western box. For instance, SSS ISV is very pronounced in the Celebes Sea and New Guinea coastal area (Figure 1), and the two regions are connected with the western equatorial PO via the NECC and NGCC. To test this hypothesis, we calculate the 20–90 day ADV using the NoSeason output. Its STD in May–August is 0.0033 psu/d, which is smaller than the corresponding 0.0047 psu/d value in MR, and the difference is statistically significant at 95% confidence level according to a two-tailed *F* test. In addition, enhanced regional circulation also gives rise to stronger ocean internal instabilities, which may also enhance SSS ISV. Therefore, seasonal variation of ocean circulation is likely one of the origins of SSS ISV seasonality. The complicated situation in this region demands further investigation.

4. Summary and Discussion

In this study, we investigate intraseasonal (20–90 day) SSS variability in the western tropical PO by analyzing Aquarius/SAC-D SSS data and performing HYCOM experiments. Strong SSS ISV with a STD of 0.12–0.20 psu is detected in the western PO between 10°S and 10°N (Figure 1). In the high-STD region, SSS variations are not spatially uniform but exhibit complex spatial structures. Characteristics and mechanisms of SSS ISV show evident spatial variations. The observed SSS variations are well simulated by HYCOM forced by the high-quality satellite atmospheric data for the 2002–2011 period. Comparisons with satellite and in-situ observational data suggest that HYCOM can reasonably represent the upper-ocean processes associated with SSS ISV in the western tropical PO.

Six parallel HYCOM experiments were performed to isolate effects of different processes. Surface forcing by atmospheric intraseasonal oscillations, referred to as the MJO forcing because of its dominance, is responsible for most of the SSS ISV. The MJO-forced SSS variability has similar amplitude to, and is highly correlated with, the total SSS ISV. The effect of ocean internal (unforced) variability plays a minor role. The MJO forcing effects through precipitation, wind stress, and wind speed are separately evaluated. The results suggest that precipitation and wind stress-driven oceanic processes (horizontal advection and vertical entrainment) are the two major drivers of SSS ISV. They have comparable influence in the equatorial PO west of 155°E and in the southwestern tropical PO. Wind stress effect dominates SSS ISV in the equatorial PO east of 155°E (eastern box of Figure 2), while precipitation effect is larger in magnitude in the northwestern tropical PO (northern box). Wind speed effect through evaporation also has large magnitude, but it is negatively correlated with the total SSS ISV. Further analysis suggests that wind stress affects mixed-layer salinity variability mainly through horizontal advection and to a lesser degree through vertical entrainment. Advection is especially important in the equatorial PO east of 155°E, where wind stress effect dominates precipitation effect due to the strong wind-driven anomalous currents and large mean SSS gradient.

The SSS ISV also exhibits strong seasonality in some areas, particularly in the western and southern boxes. In boreal winter, SSS ISV is reduced in the northern hemisphere and enhanced in the southern hemisphere, while in boreal summer the pattern is reversed. There are mainly two factors influencing this seasonality, i.e., the strength of MJO forcing and the ocean background state. Effects of the two factors are separated by the HYCOM NoSeason experiment in which seasonal and interannual variations in the ocean state are removed. The SSS ISV seasonality in NoSeason is much smaller than that in HYCOM MR, indicating that seasonal variation of ocean state plays a more important role in regulating the seasonality of SSS ISV.

Particularly, the seasonal variation of MLD can explain much of the ISV amplitude changes. A thinner (thicker) mixed layer leads to stronger (weaker) SSS ISV in response to various forcing processes. This effect however does not work in the western box, particularly for the large intensification of SSS ISV during May–August. The seasonality of SSS ISV during this season is likely affected by seasonal intensification of ocean currents and the interactions between ocean variation and atmospheric forcing.

Our results suggest that at seasonal timescale, amplitude of SSS ISV is more sensitive to the ocean state rather than to the MJO strength. This result indicates that realistic representation of the ocean background state, such as the MLD, thermocline, and upper-ocean circulation, is crucial for the model simulation of the mixed layer variability (e.g., SSS and SST) in response to the MJO. At present, the state-of-the-art climate models still have difficulties in realistically simulating and forecasting the MJO behaviors and the related SST variability [e.g., *Lin et al*., 2006; *Xavier*, 2012; *Hung et al*., 2013]. A more realistic ocean state will probably improve the representation of intraseasonal variability of SST and SSS and their feedbacks to the MJO. Strong SSS variability at intraseasonal timescales described in this study also implies variability in the upper-ocean salt stratification. The existence and variability of the salt-stratified barrier layer play a vital role in the mixed layer heat budget of the western PO warm pool region [e.g., *Sprintall and Tomczak*, 1992; *Maes et al*., 2005]. Intraseasonal variability of barrier layer in the western tropical PO has not yet been explored. How the barrier layer thickness varies during the MJO, what processes govern its variability, and to what extent it influences SST variability are interesting themes for our future research.

Acknowledgments

This research receives supports from the NASA Ocean Salinity Science Team award NNX14AI82G, NASA Ocean Vector Wind Science Team award NNX14AM68G, and NOAA NA11OAR4310100. Two anonymous reviewers provided important comments for improving our work. We appreciate the National Center for Atmospheric Research (NCAR) CISL and the Office of Information Technology (OIT) of University of Colorado and for providing and maintaining the computational resource. Aquarius CAP and CAP-RC Level 3 Version 3.0 SSS data are distributed by PO.DAAC and accessible through the FTP site ftp://podaac-ftp.jpl.nasa.gov/allData/aquarius/; MOAA GPV data are provided by Dr. Shigeki Hosoda through the FTP site ftp://ftp2.jamstec.go.jp/pub/argo/MOAA_GPV/; TRMM TMPA level 3B42 precipitation product is available at http://mirador.gsfc.nasa.gov/; CCMP sea surface wind data are downloaded from http://podaac.jpl.nasa.gov/; OSCAR ocean surface current data are available at http://www.oscar.noaa.gov/; the real-time multivariate MJO (RMM) index is obtained from the Centre for Australian Weather and Climate Research through http://cawcr.gov.au/staff/mwheeler/maproom/RMM/; data processing and graphing work in this study are finished with a licensed Matlab program.

References

Antonov, J. I., D. Seidov, T. P. Boyer, R. A. Locarnini, A. V. Mishonov, H. E. Garcia, O. K. Baranova, M. M. Zweng, and D. R. Johnson (2010), Volume 2: Salinity, in *World Ocean Atlas 2009, NOAA Atlas NESDIS 69*, edited by S. Levitus, 184 pp., U.S. Gov. Print. Off., Washington, D. C.

Atlas, R., J. Ardizzone, and R. N. Hoffman (2008), Application of satellite surface wind data to ocean wind analysis, *Proc. SPIE*, *7087*, 70870B, doi:10.1117/12.795371.

Bingham, F. M., J. Busecke, A. L. Gordon, C. F. Giulivi, and Z. Li (2014), The North Atlantic subtropical surface salinity maximum as observed by Aquarius, *J. Geophys. Res. Oceans*, *119*, 7741–7755, doi:10.1002/2014JC009825.

Bleck, R. (2002), An oceanic general circulation model framed in hybrid isopycnic-Cartesian coordinates, *Ocean Modell.*, *4*, 55–88.

Bonjean, F., and G. S. Lagerloef (2002), Diagnostic model and analysis of the surface currents in the tropical Pacific Ocean, *J. Phys. Oceanogr.*, *32*(10), 2938–2954.

Cravatte, S., T. Delcroix, D. Zhang, M. McPhaden, and J. Leloup (2009), Observed freshening and warming of the western Pacific warm pool, *Clim. Dyn.*, *33*(4), 565–589.

de Boyer Montégut, C., G. Madec, A. S. Fischer, A. Lazar, and D. Iudicone (2004), Mixed layer depth over the global ocean: An examination of profile data and a profile-based climatology, *J. Geophys. Res.*, *109*, C12003, doi:10.1029/2004JC002378.

Dee, D., S. Uppala, A. Simmons, P. Berrisford, P. Poli, S. Kobayashi, U. Andrae, M. Balmaseda, G. Balsamo, and P. Bauer (2011), The ERA-Interim reanalysis: Configuration and performance of the data assimilation system, *Q. J. R. Meteorol. Soc.*, *137*, 553–597.

Delcroix, T., and C. Henin (1991), Seasonal and interannual variations of sea surface salinity in the tropical Pacific Ocean, *J. Geophys. Res.*, *96*(C12), 22,135–22,150.

Delcroix, T., and M. McPhaden (2002), Interannual sea surface salinity and temperature changes in the western Pacific warm pool during 1992–2000, *J. Geophys. Res.*, *107*(C12), 8002, doi:10.1029/2001JC000862.

Delcroix, T., and J. Picaut (1998), Zonal displacement of the western equatorial Pacific ''fresh pool,'' *J. Geophys. Res.*, *103*(C1), 1087–1098.

Delcroix, T., C. Hénin, V. Porte, and P. Arkin (1996), Precipitation and sea-surface salinity in the tropical Pacific Ocean, *Deep Sea Res., Part I*, *43*(7), 1123–1141.

Delcroix, T., S. Cravatte, and M. J. McPhaden (2007), Decadal variations and trends in tropical Pacific sea surface salinity since 1970, *J. Geophys. Res.*, *112*, C03012, doi:10.1029/2006JC003801.

Delcroix, T., M.-H. Radenac, S. Cravatte, G. Alory, L. Gourdeau, F. Léger, A. Singh, and D. Varillon (2014), Sea surface temperature and salinity seasonal changes in the western Solomon and Bismarck Seas, *J. Geophys. Res. Oceans*, *119*, 2642–2657, doi:10.1002/2013JC009733.

Dohan, K., H.-Y. Kao, and G. S. Lagerloef (2015), The freshwater balance over the North Atlantic SPURS domain from Aquarius satellite salinity, OSCAR satellite surface currents, and some simplified approaches, *Oceanography*, *28*(1), 86–95.

Duchon, C. E. (1979), Lanczos filtering in one and two dimensions, *J. Appl. Meteorol.*, *18*, 1016–1022.

Duncan, B., and W. Han (2012), Influence of atmospheric intraseasonal oscillations on seasonal and interannual variability in the upper Indian Ocean, *J. Geophys. Res.*, *117*, C11028, doi:10.1029/2012JC008190.

Felton, C. S., B. Subrahmanyam, V. S. N. Murty, and J. F. Shriver (2014), Estimation of the barrier layer thickness in the Indian Ocean using Aquarius Salinity, *J. Geophys. Res. Oceans*, *119*, 4200–4213, doi:10.1002/2013JC009759.

Font, J., A. Camps, A. Borges, M. Martín-Neira, J. Boutin, N. Reul, Y. H. Kerr, A. Hahne, and S. Mecklenburg (2010), SMOS: The challenging sea surface salinity measurement from space, *Proc. IEEE*, *98*(5), 649–665.

Gierach, M. M., J. Vazquez-Cuervo, T. Lee, and V. M. Tsontos (2013), Aquarius and SMOS detect effects of an extreme Mississippi River flooding event in the Gulf of Mexico, *Geophys. Res. Lett.*, *40*, 5188–5193, doi:10.1002/grl.50995.

Gouriou, Y., and J. Toole (1993), Mean Circulation of the Upper Layers of the Western Equatorial Pacific Ocean, *J. Geophys. Res.*, *98*(C12), 22,495-22,520.

Grodsky, S. A., G. Reverdin, J. A. Carton, and V. J. Coles (2014), Year-to-year salinity changes in the Amazon plume: Contrasting 2011 and 2012 Aquarius/SACD and SMOS satellite data, *Remote Sens. Environ.*, *140*, 14–22.

Grunseich, G., B. Subrahmanyam, and B. Wang (2013), The Madden-Julian oscillation detected in Aquarius salinity observations, *Geophys. Res. Lett.*, *40*, 5461–5466, doi:10.1002/2013GL058173.

Guan, B., T. Lee, D. J. Halkides, and D. E. Waliser (2014), Aquarius surface salinity and the Madden-Julian Oscillation: The role of salinity in surface layer density and potential energy, *Geophys. Res. Lett.*, *41*, 2858–2869, doi:10.1002/2014GL059704.

Hasson, A., T. Delcroix, J. Boutin, R. Dussin, and J. Ballabrera-Poy (2014), Analyzing the 2010–2011 La Niña signature in the tropical Pacific sea surface salinity using in situ data, SMOS observations, and a numerical simulation, *J. Geophys. Res. Oceans*, *119*, 3855–3867, doi:10.1002/2013JC009388.

Hasson, A. E., T. Delcroix, and R. Dussin (2013), An assessment of the mixed layer salinity budget in the tropical Pacific Ocean. Observations and modelling (1990–2009), *Ocean Dyn.*, *63*(2-3), 179–194.

Hénin, C., Y. du Penhoat, and M. Ioualalen (1998), Observations of sea surface salinity in the western Pacific fresh pool: Large-scale changes in 1992–1995, *J. Geophys. Res.*, *103*(C4), 7523–7536.

Hosoda, S., T. Ohira, and T. Nakamura (2008), A monthly mean dataset of global oceanic temperature and salinity derived from Argo float observations, *JAMSTEC Rep. Res. Dev.*, *8*, 47–59.

Hsin, Y. C., and B. Qiu (2012), Seasonal fluctuations of the surface North Equatorial Countercurrent (NECC) across the Pacific basin, *J. Geophys. Res.*, *117*, C06001, doi:10.1029/2011JC007794.

Huffman, G. J., D. T. Bolvin, E. J. Nelkin, D. B. Wolff, R. F. Adler, G. Gu, Y. Hong, K. P. Bowman, and E. F. Stocker (2007), The TRMM Multisatellite Precipitation Analysis (TMPA): Quasi-Global, Multiyear, Combined-Sensor Precipitation Estimates at Fine Scales, *J. Hydrometeorol.*, *8*(1), 38–55.

Hung, M.-P., J.-L. Lin, W. Wang, D. Kim, T. Shinoda, and S. J. Weaver (2013), MJO and convectively coupled equatorial waves simulated by CMIP5 climate models, *J. Clim.*, *26*(17), 6185–6214.

Ioualalen, M., Y. Wakata, Y. Kawahara, Y. Gouriou, and D. Varillon (2003), Variability of the sea surface salinity (SSS) in the western tropical Pacific: On the ability of an OGCM to simulate the SSS, and on the sampling of an operating merchant ship SSS network, *J. Oceanogr.*, *59*(1), 105–111.

Jochum, M., and R. Murtugudde (2005), Internal variability of Indian ocean SST, *J. Clim.*, *18*(18), 3726–3738.

Johnson, G. C., B. M. Sloyan, W. S. Kessler, and K. E. McTaggart (2002), Direct measurements of upper ocean currents and water properties across the tropical Pacific during the 1990s, *Prog. Oceanogr.*, *52*(1), 31–61.

Kao, H.-Y., and G. S. E. Lagerloef (2015), Salinity fronts in the tropical Pacific Ocean, *J. Geophys. Res. Oceans*, *120*(2), 1096–1106. doi:10.1002/2014jc010114.

Kara, A. B., H. E. Hurlburt, and A. J. Wallcraft (2005), Stability-dependent exchange coefficients for air-sea fluxes, *J. Atmos. Oceanic Technol.*, *22*, 1080–1094.

Kashino, Y., A. Ishida, and S. Hosoda (2011), Observed ocean variability in the Mindanao Dome region, *J. Phys. Oceanogr.*, *41*, 287–302.

Kiladis, G. N., M. C. Wheeler, P. T. Haertel, K. H. Straub, and P. E. Roundy (2009), Convectively coupled equatorial waves, *Rev. Geophys.*, *47*, RG2003, doi:10.1029/2008RG000266.

Kim, S.-B., J.-H. Lee, P. de Matthaeis, S. Yueh, C.-S. Hong, J.-H. Lee, and G. Lagerloef (2014), Sea surface salinity variability in the East China Sea observed by the Aquarius instrument, *J. Geophys. Res. Oceans*, *119*, 7016–7028, doi:10.1002/2014JC009983.

Kuroda, Y. (2000), Variability of the currents off the north coast of New Guinea, *J. Oceanogr.*, *56*, 103–106.

Lagerloef, G. S. E, C. Swift, and D. Le Vine (1995), Sea surface salinity: The next remote sensing challenge, *Oceanography*, *8*(2), 44–50.

Lagerloef, G. S. E., et al. (2008), The Aquarius/SAC-D mission, *Oceanography*, *21*, 68–81.

Lee, T., G. Lagerloef, M. M. Gierach, H. Y. Kao, S. Yueh, and K. Dohan (2012), Aquarius reveals salinity structure of tropical instability waves, *Geophys. Res. Lett.*, *39*, L12610, doi:10.1029/2012GL052232.

Lee, T., G. Lagerloef, H.-Y. Kao, M. J. McPhaden, J. Willis, and M. M. Gierach (2014), The influence of salinity on tropical Atlantic instability waves, *J. Geophys. Res. Oceans*, *119*, 8375–8394, doi:10.1002/2014JC010100.

Li, Y., W. Han, T. Shinoda, C. Wang, R. C. Lien, J. N. Moum, and J. W. Wang (2013), Effects of the diurnal cycle in solar radiation on the tropical Indian Ocean mixed layer variability during wintertime Madden-Julian Oscillations, *J. Geophys. Res. Oceans*, *118*, 4945–4964, doi:10.1002/jgrc.20395.

Li, Y., W. Han, T. Shinoda, C. Wang, M. Ravichandran, and J.-W. Wang (2014), Revisiting the wintertime intraseasonal SST variability in the tropical South Indian Ocean: Impact of the ocean interannual variation, *J. Phys. Oceanogr.*, *44*(7), 1886–1907.

Li, Y., W. Han, and T. Lee (2015), Intraseasonal sea surface salinity variability in the equatorial Indo-Pacific Ocean induced by Madden-Julian oscillations, *J. Geophys. Res. Oceans*, *120*, 2233–2258, doi:10.1002/2014JC010647.

Lin, J. L., et al. (2006), Tropical intraseasonal variability in 14 IPCC AR4 climate models. Part I: Convective signals, *J. Clim.*, *19* 2665–2690.

Lindstrom, E., R. Lukas, R. Fine, E. Firing, S. Godfrey, G. Meyers, and M. Tsuchiya (1987), The western equatorial Pacific Ocean circulation study, *Nature*, *330*(10), 533–537.

Locarnini, R. A., A. V. Mishonov, J. I. Antonov, T. P. Boyer, H. E. Garcia, O. K. Baranova, M. M. Zweng, and D. R. Johnson (2010), Volume 1: Temperature, in *World Ocean Atlas 2009, NOAA Atlas NESDIS 68*, 184 pp., edited by S. Levitus, U.S. Gov. Print. Off., Washington, D. C.

Loeb, N. G., K. J. Priestley, D. P. Kratz, E. B. Geier, R. N. Green, B. A. Wielicki, P. O. R. Hinton, and S. K. Nolan (2001), Determination of unfiltered radiances from the clouds and the Earth's radiant energy system instrument, *J. Appl. Meteorol.*, *40*, 822–835.

Lukas, R., and E. Lindstrom (1991), The mixed layer of the western equatorial Pacific Ocean, *J. Geophys. Res.*, *96*(S01), 3343–3357.

Madden, R. A., and P. R. Julian (1971), Detection of a 40–50 day oscillation in the zonal wind in the tropical Pacific, *J. Atmos. Sci.*, *28*, 702–708.

Maes, C. (2000), Salinity variability in the equatorial Pacific Ocean during the 1993-98 period, *Geophys. Res. Lett.*, *27*(11), 1659–1662.

Maes, C., J. Picaut, and S. Belamari (2005), Importance of the salinity barrier layer for the buildup of El Niño, *J. Clim.*, *18*(1), 104–118.

Matthews, A. J., P. Singhruck, and K. J. Heywood (2010), Ocean temperature and salinity components of the Madden–Julian oscillation observed by Argo floats, *Clim. Dyn.*, *35*(7), 1149–1168.

Moon, J.-H., and Y. T. Song (2014), Seasonal salinity stratifications in the near-surface layer from Aquarius, Argo, and an ocean model: Focusing on the tropical Atlantic/Indian Oceans, *J. Geophys. Res. Oceans*, *119*, 6066–6077, doi:10.1002/2014JC009969.

North, G. R., T. L. Bell, R. F. Cahalan, and F. J. Moeng (1982), Sampling errors in the estimation of empirical orthogonal functions, *Mon. Weather Rev.*, *110*(7), 699–706.

Picaut, J., M. Ioualalen, C. Menkès, T. Delcroix, and M. McPhaden (1996), Mechanism of the zonal displacements of the Pacific warm pool: Implications for ENSO, *Science*, *274*(5292), 1486–1489.

Qiu, B. (1999), Seasonal eddy field modulation of the North Pacific Subtropical Countercurrent: TOPEX/Poseidon observations and theory, *J. Phys. Oceanogr.*, *29*(10), 2471–2486.

Qu, T., and J.-Y. Yu (2014), ENSO indices from sea surface salinity observed by Aquarius and Argo, *J. Oceanogr.*, *70*(4), 367–375.

Qu, T., Y. T. Song, and C. Maes (2014), Sea surface salinity and barrier layer variability in the equatorial Pacific as seen from Aquarius and Argo, *J. Geophys. Res. Oceans*, *119*, 15–29, doi:10.1002/2013JC009375.

Reul, N., B. Chapron, T. Lee, C. Donlon, J. Boutin, and G. Alory (2014), Sea surface salinity structure of the meandering Gulf Stream revealed by SMOS sensor, *Geophys. Res. Lett.*, *41*, doi:10.1002/2014GL059215.

Sabia, R., M. Klockmann, D. Fernández-Prieto, and C. Donlon (2014), A first estimation of SMOS-based ocean surface T-S diagrams, *J. Geophys. Res. Oceans*, *119*, 7357–7371, doi:10.1002/2014JC010120.
Shinoda, T., T. Jensen, M. Flatau, W. Han, and C. Wang (2013), Large-scale oceanic variability associated with the Madden-Julian oscillation during the CINDY/DYNAMO field campaign from satellite observations, *Remote Sens.*, *5*, 2072–2092.
Singh, A., T. Delcroix, and S. Cravatte (2011), Contrasting the flavors of El Niño-Southern Oscillation using sea surface salinity observations, *J. Geophys. Res.*, *116*, C06016, doi:10.1029/2010JC006862.
Skliris, N., R. Marsh, S. Josey, S. Good, C. Liu, and R. Allan (2014), Salinity changes in the World Ocean since 1950 in relation to changing surface freshwater fluxes, *Clim. Dyn.*, *43*(3-4), 709–736.
Song, Y. T., T. Lee, J.-H. Moon, T. Qu, and S. Yueh (2015), Modeling skin-layer salinity with an extended surface-salinity layer, *J. Geophys. Res. Oceans*, *120*, 1079–1095, doi:10.1002/2014JC010346.
Sprintall, J., and M. Tomczak (1992), Evidence of the barrier layer in the surface layer of the tropics, *J. Geophys. Res.*, *97*(C5), 7305–7316.
Stevenson, J. W., and P. P. Niiler (1983), Upper ocean heat budget during the Hawaii-to-Tahiti shuttle experiment, *J. Phys. Oceanogr.*, *13*(10), 1894–1907.
Tang, W., S. H. Yueh, A. G. Fore, A. Hayashi, T. Lee, and G. Lagerloef (2014), Uncertainty of Aquarius sea surface salinity retrieved under rainy conditions and its implication on the water cycle study, *J. Geophys. Res. Oceans*, *119*, 4821–4839, doi:10.1002/2014JC009834.
Ueki, I., K. Ando, Y. Kuroda, and K. Kutsuwada (2002), Salinity variation and its effect on dynamic height along the 156° E in the Pacific warm pool, *Geophys. Res. Lett.*, *29*(14), 1689, doi:10.1029/2001GL013993.
Ueki, I., Y. Kashino, and Y. Kuroda (2003), Observation of current variations off the New Guinea coast including the 1997–1998 El Niño period and their relationship with Sverdrup transport, *J. Geophys. Res.*, *108*(C7), 3243, doi:10.1029/2002JC001611.
Wang, X., and Y. Chao (2004), Simulated Sea Surface Salinity variability in the tropical Pacific, *Geophys. Res. Lett.*, *31*, L02302, doi:10.1029/2003GL018146.
Wheeler, M., and G. N. Kiladis (1999), Convectively coupled equatorial waves: Analysis of clouds and temperature in the wavenumber-frequency domain, *J. Atmos. Sci.*, *56*, 374–399.
Wheeler, M. C., and H. H. Hendon (2004), An all-season real-time multivariate MJO index: Development of an index for monitoring and prediction, *Mon. Weather Rev.*, *132*, 1917–1932.
Wielicki, B. A., B. R. Barkstrom, E. F. Harrison, R. B. Lee III, G. Louis Smith, and J. E. Cooper (1996), Clouds and the Earth's Radiant Energy System (CERES): An earth observing system experiment, *Bull. Am. Meteorol. Soc.*, *77*, 853–868.
Xavier, P. K. (2012), Intraseasonal convective moistening in CMIP3 models, *J. Clim.*, *25*, 2569–2577.
Yaremchuk, M., and T. Qu (2004), Seasonal variability of the large-scale currents near the coast of the Philippines, *J. Phys. Oceanogr.*, *34*(4), 844–855.
Yu, L. (2011), A global relationship between the ocean water cycle and near-surface salinity, *J. Geophys. Res.*, *116*, C10025, doi:10.1029/2010JC006937.
Yu, L. (2014), Coherent evidence from Aquarius and Argo for the existence of a shallow low-salinity convergence zone beneath the Pacific ITCZ, *J. Geophys. Res. Oceans*, *119*, 7625–7644, doi:10.1002/2014JC010030.
Yu, L. (2015), Sea-surface salinity fronts and associated salinity-minimum zones in the tropical ocean, *J. Geophys. Res. Oceans*, *120*, 4205–4225, doi:10.1002/2015JC010790.
Yueh, S., W. Tang, A. Fore, A. Hayashi, Y. T. Song, and G. Lagerloef (2014), Aquarius geophysical model function and combined active passive algorithm for ocean surface salinity and wind retrieval, *J. Geophys. Res. Oceans*, *119*, 5360–5379, doi:10.1002/2014JC009939.
Yueh, S. H., W. Tang, A. G. Fore, G. Neumann, A. Hayashi, A. Freedman, J. Chaubell, and G. S. Lagerloef (2013), L-band passive and active microwave geophysical model functions of ocean surface winds and applications to Aquarius retrieval, *IEEE Trans. Geosci. Remote Sens.*, *51*(9), 4619–4632.
Zeng, L., W. Timothy Liu, H. Xue, P. Xiu, and D. Wang (2014), Freshening in the South China Sea during 2012 revealed by Aquarius and in situ data, *J. Geophys. Res. Oceans*, *119*, 8296–8314, doi:10.1002/2014JC010108.
Zhang, C. (2005), Madden-Julian oscillation, *Rev. Geophys.*, *43*, RG2003, doi:10.1029/2004RG000158.
Zhou, L., R. Murtugudde, and M. Jochum (2008), Dynamics of the intraseasonal oscillations in the Indian Ocean South Equatorial Current, *J. Phys. Oceanogr.*, *38*(1), 121–132.
Zhu, J., B. Huang, R.-H. Zhang, Z.-Z. Hu, A. Kumar, M. A. Balmaseda, L. Marx, and J. L. Kinter Iii (2014), Salinity anomaly as a trigger for ENSO events, *Sci. Rep.*, *4*, 6821, doi:10.1038/srep06821.